Physics of Fluids, Volume 36, Issue 8, August 2024, Article number 085199
DOI:10.1063/5.0222780

Performance Analyses of Active Aerodynamic Load Balancing Designs on High-Performance Vehicles in Cornering Conditions

Steven Rijns[a,*], Tom-Robin Teschner[b], Kim Blackburn[a], James Brighton[a]

[a]*Advanced Vehicle Engineering Centre, Cranfield University, Cranfield, MK43 0AL, United Kingdom*
[b]*Centre for Computational Engineering Sciences, Cranfield University, Cranfield, MK43 0AL, United Kingdom*

Abstract

This study presents a comprehensive investigation into the impact of Active Aerodynamic Load Balancing (AALB) on the cornering performance of high-performance vehicles. The research explores the use of active asymmetric aerodynamic devices, specifically split and tilted rear wing concepts, capable of manipulating vertical wheel loads and counteracting effects of lateral load transfer during cornering. The performance potential of AALB is assessed through quasi-steady static coupling of aerodynamic data with a detailed vehicle dynamics model. The findings show that inside bias operating states of the split rear wing and tilted rear wing concepts, which favour loads on the inside tyres, can improve cornering velocities up to 0.5% and 2% compared to high symmetric operating states, respectively. Noteworthy, through effective distribution of aerodynamic loads, the inside bias operating states produce less downforce and drag, thereby reducing the propulsion power required to overcome drag by 15%-20%, depending on the cornering condition. The tilted rear wing concept demonstrates the highest AALB capability and most consistent response to its control strategy, accredited to its ability to generate vertical and horizontal aerodynamic force components. It can therefore achieve over 1% higher maximum cornering velocities compared to the split rear wing, while also offering efficiency benefits. Overall, the research highlights the effectiveness of AALB in improving cornering performance and efficiency, offering valuable insights for the development of advanced active aerodynamic solutions in automotive design and paving the way for future advancements in the field.

1. Introduction

Aerodynamics is a critical factor in the design of high-performance and motorsport vehicles, significantly impacting performance, efficiency, and handling in dynamic operating conditions such as cornering. During cornering, an outward-directed centrifugal force acts on the vehicle's centre of gravity, instigating a load transfer from the inside to the outside tyres. Due to the non-linear vertical load sensitivity of tyres, this lateral load transfer reduces the potential combined lateral force produced by the tyres on each axle. Excessive load transfer can even overload the tyres, thereby drastically reducing grip and compromising cornering performance (Seward (2014), Dixon (1996)).

The research objectives of this study originate from the hypothesis that reducing lateral load transfer from the inside to the outside tyres during cornering can enhance the overall grip produced by the tyres. The proposed Active Aerodynamic Load Balancing (AALB) approach focuses on generating aerodynamic loads which favour vertical forces on the inside tyres and induce an aerodynamic roll moment which opposes the overturning moment resulting from the centrifugal force in cornering conditions.

*Corresponding author at: Advanced Vehicle Engineering Centre, Cranfield University, Cranfield, MK43 0AL, United Kingdom.
Email address: steven.rijns@cranfield.ac.uk

Such advanced aerodynamic solutions can potentially offer greater benefits than conventional modifications to the vehicle's suspension system, tyre design, or centre of gravity position, which can only redistribute or partially mitigate load transfer and are limited by inherent design constraints.

Research has demonstrated that the aerodynamic performance of vehicles is significantly impacted during cornering as well. Studies focused on automotive applications have revealed notable changes in surface pressure distributions and wake characteristics in cornering conditions, which in turn affect aerodynamic lift, drag, and side forces (Keogh (2016), Keogh et al. (2016), Nakashima et al. (2020), Heft et al. (2012), Josefsson et al. (2018), Nakashima et al. (2015), Kono et al. (2016)).

High-performance and motorsport vehicles exhibit heightened sensitivity to these conditions, primarily due to their aerodynamic devices (Albukrek et al. (2006), Nara et al. (2014), Rijns et al. (2024d,b)). Downforce and drag penalties ranging from 20% to 30% have been reported for such vehicles in tight corners and yaw conditions compared to straight-line conditions.

These findings highlight the importance of analysing a diverse range of representative operating conditions to assess a vehicle's aerodynamic performance. To thoroughly investigate a vehicle's cornering performance, it is also essential to capture the interrelation between its aerodynamics and dynamics. This interplay can be examined using coupling methods of varying

Published by AIP Publishing. This is the Author Accepted Manuscript issued with: Creative Commons Attribution License (CC:BY 4.0).
The final published version (version of record) is available online at DOI:10.1063/5.0222780. Please refer to any applicable publisher terms of use.

complexity (Forbes et al. (2016)), namely quasi-steady static coupling, unsteady static coupling, and unsteady dynamic coupling.

Quasi-steady static coupling employs steady-state CFD simulations, while unsteady static coupling utilises transient CFD simulations on a vehicle with a fixed position as input to a vehicle dynamics model. Unsteady dynamic coupling, the most complex method, iterates between CFD simulations and a vehicle dynamics model to continuously update changes in the vehicle's position and aerodynamic loads. However, the increased complexity of these methods results in a significant trade-off in computational time and resources.

Various coupling methods have been employed for automotive applications to investigate the stability and handling of passenger vehicles and large trucks during dynamic events such as crosswind gusts (Tunay et al. (2018), Tunay (2023), Forbes (2017), Adam Brandt and Sebben (2022), Nakashima et al. (2011)). Comparative studies have highlighted the trade-off between computational efficiency and accuracy among these methods (Forbes et al. (2016), Winkler et al. (2016), Nakashima et al. (2013), Carbonne et al. (2016)). While results vary, fully coupled methods generally benefit large vehicles in severe conditions despite higher computational costs, whereas one-way coupling methods can suffice for smaller passenger vehicles.

The impact of aerodynamic devices on vehicle performance has been predominately investigated with quasi-steady static coupling methods. A majority of the studies have employed aerodynamic data from isolated devices (Mckay and Gopalarathnam (2002), Hammad et al. (2019), Ahangarnejad and Melzi (2018), Diba et al. (2014)), while others have taken the aerodynamics of the entire vehicle into account (Lin and Papadopoulos (2022), Cai et al. (2017)). The consensus among these findings is that aerodynamic devices contribute to enhancements in cornering performance and stability.

More intricate fully coupled analyses involving a vehicle equipped with various aerodynamic add-on devices have also reported improvements in cornering performance, a finding corroborated by road tests (Kurec et al. (2019a)). Subsequent investigations on the same vehicle have demonstrated a reduction in braking distance and an improvement in stability during straight-line braking and brake-in-turn events using an active rear wing (Broniszewski and Piechna (2019, 2022)).

Other studies have similarly demonstrated promising results for active aerodynamic devices on vehicles, indicating further potential benefits. Small spoiler plates underneath larger spoilers or rear wings have been shown to enhance downforce generation, benefiting from faster actuation (Kurec et al. (2019b), Piechna et al. (2022)). Findings on asymmetric active devices have revealed that split rear wings can vary the downforce on the inside and outside tires, but primarily affect the rear tyres (Sikder et al. (2016), Ayyagari and He (2017)). Similarly, tilted rear wings can effectively generate downforce and side force, influencing the lateral distribution of vertical tyre loads (Piechna et al. (2022), Zavala et al. (2023)).

Road tests of vehicles equipped with tilted rear wings have demonstrated an approximate 13% increase in cornering velocity compared to a configuration without aerodynamic devices (Piechna et al. (2022)). However, most studied active devices produced rear axle downforce, resulting in an aerodynamically unbalanced vehicle. While splitters were found to partially generate the necessary downforce, more substantial amounts of front axle downforce was generated with front wings, thereby having the potential to provide balanced loads for large active rear wings (Szudarek and Piechna (2021)).

The reviewed studies have underscored the effectiveness of coupled simulations in analysing the complex interrelation between vehicle aerodynamics and dynamics, and similarly highlighted the potential benefits of active aerodynamic devices on vehicles. Building on this previous work, the present research delves deeper into the use of active asymmetric aerodynamic devices and their capabilities of influencing the aerodynamic load distribution to enhance cornering performance, an area previously underexplored.

A key focus of this study is to explore the performance potential of asymmetrically distributing aerodynamic loads across the inside and outside tyres, while maintaining a balanced front-to-rear distribution, referred to as Active Aerodynamic Load Balancing (AALB). This innovative approach aims prioritise vertical loads on the inside tyres and counteract effects of lateral load transfer, with the goal of improving overall grip and thereby enhancing cornering performance.

To achieve this, the study employs active split rear wing and tilted rear wing concepts. In conjunction with an active split front wing, these concepts have the potential to manipulate the vehicle's longitudinal and lateral aerodynamic balance. Quasi-steady static coupling of extensive aerodynamic data sets across a variety of cornering conditions with a detailed vehicle dynamics model is utilised to assess cornering performance. Through this comprehensive investigation, the research aims to provide valuable insights in the AALB capability of different active asymmetric aerodynamic solutions and their effectiveness in improving cornering performance.

2. Methodology

This research is based on the hypothesis that generating aerodynamic loads which promote downforce on the inside tyres and oppose the overturning moment from the centrifugal force can improve the vehicle's overall grip during cornering. The proposed AALB principle is achieved through the design of two high-performance vehicle concepts using promising active aerodynamic solutions identified in existing literature.

The influence of the AALB on cornering performance is investigated using quasi-steady static coupling of the vehicle's aerodynamics and dynamics. This method employs a one-way coupling of aerodynamic data as input for a vehicle dynamics model. Conventionally, aerodynamic data is often generated in straight-line conditions due to the absence of prior knowledge on vehicle performance. However, our previous work has underscored the significant influence of operating conditions on the aerodynamic performance of high-performance vehicles (Rijns et al. (2024d,b)), indicating that straight-line aerodynamic data may not accurately reflect the aerodynamic performance in dynamic events such as cornering.

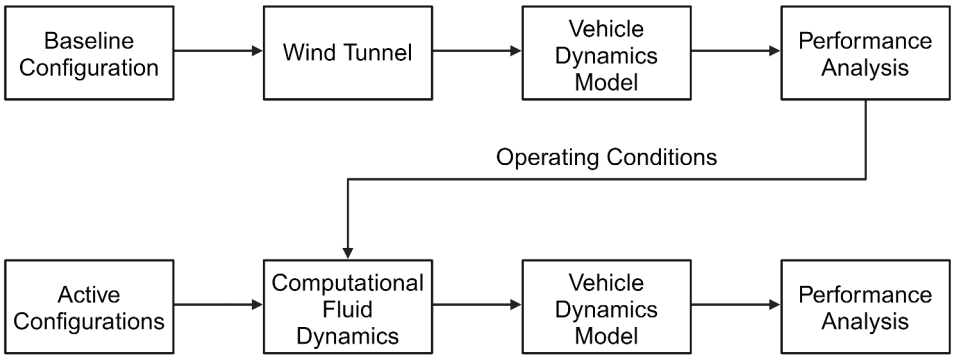


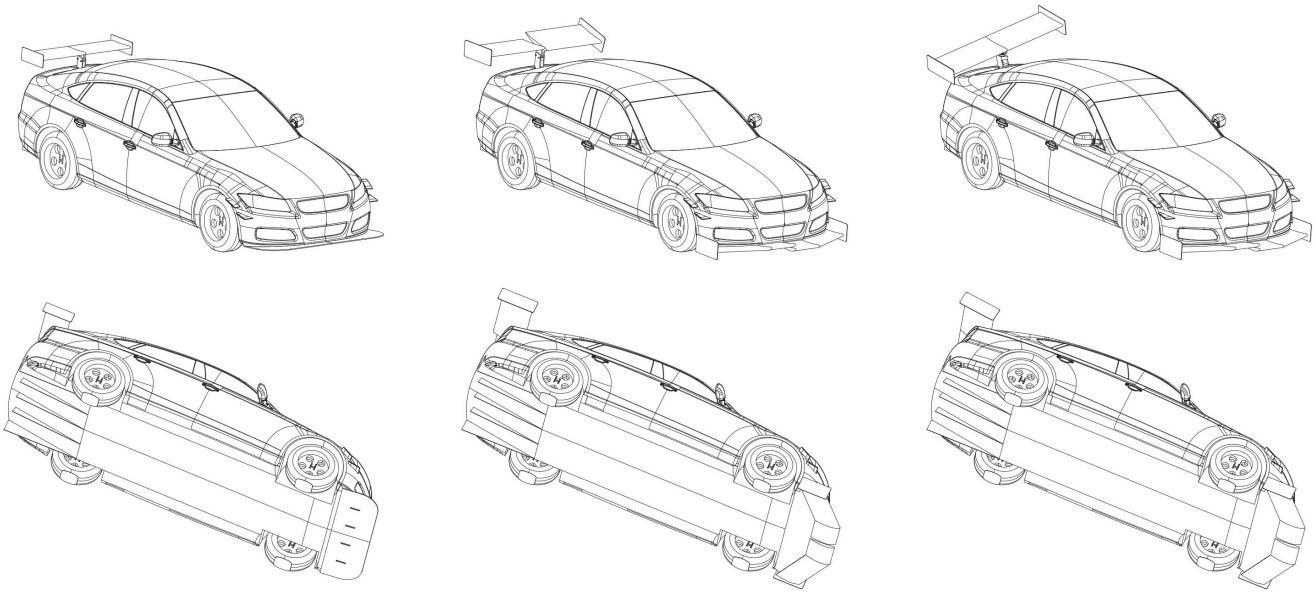
Figure 1: Research process flowchart

A key focus of the methodology is therefore the generation of aerodynamic data across a range of representative operating conditions. The research process, outlined in Figure 1, commences with an initial performance assessment using wind tunnel data of an existing high-performance vehicle, which serves as the baseline geometry in this study. This initial performance assessment is used to determine representative operating conditions for the CFD simulations on the active high-performance vehicle concepts. Successively, the vehicle dynamics model uses the simulated aerodynamic data to examine the cornering performance of the active high-performance vehicle concepts. The subsequent sections of the methodology will detail the vehicle geometry, wind tunnel experiments, CFD simulations, and vehicle dynamics model employed throughout the study.

2.1. Vehicle Geometry

The *DrivAer hp-F* vehicle model, a high-performance variant of the well-established DrivAer model (Heft et al. (2012)), serves as the baseline geometry for this study. Specifically developed for aerodynamic research on high-performance vehicles (Soares et al. (2018)), the *DrivAer hp-F* model features a smooth underbody and is equipped with additional aerodynamic elements. These elements include a 41 mm front bumper splitter, forebody strakes, a 10° underbody multichannel diffuser, and a NACA 6412 profile rear wing, as depicted in Figure 2a.

This study introduces two high-performance vehicle concepts based on the *DrivAer hp-F*, each incorporating active aerodynamic devices for AALB. The first concept features a split rear wing, with left and right elements capable of independently adjusting their angle of attack from 0° to 30°. The



(a) (b) (c)

Figure 2: (a) baseline vehicle: *DrivAer hp-F* with standard rear wing, (b) split wing concept: *DrivAer hp-F* with active split front wing and split rear wing, and (c) tilted wing concept: *DrivAer hp-F* with active split front wing and tilted rear wing. The two active high-performance vehicle concepts are depicted in an asymmetric operating setting to illustrate the designs

second concept utilises a rear wing that can adjust both its angle of attack between 0° and 30°, and roll angle between 0° and ±12°, referred to as the tilted rear wing concept.

To maintain aerodynamic balance, both active high-performance vehicle concepts feature a split front wing, consisting of left and right elements that can independently vary their angle of attack from 0° to 10°. The active high-performance vehicle concepts are illustrated in Figure 2, and their main dimensions are listed alongside those of the baseline high-performance vehicle in Table 1.

2.2. Wind Tunnel Experiments

The experimental data from previously conducted wind tunnel tests by Rijns et al. (2024b) on the *DrivAer hp-F* model in the closed return 8x6 Wind Tunnel at Cranfield University is used in this study to provide an initial performance assessment for the CFD simulations on the active high-performance vehicle concepts. The experiments were carried out on a 35% scale model of the baseline *DrivAer hp-F* model with rear wing. The model's main dimensions are listed in Table 1 and the vehicle configuration is illustrated in full scale in Figure 2a.

The 8x6 Wind Tunnel at Cranfield University has a rectangular test section, which is 2.44 mm wide, 1.83 m high, and 5.18 m long. The experimental setup, presented in Figure 3, was equipped a moving ground facility and two-stage boundary layer suction system to optimise the ground plane boundary layer.

The experimental data includes measurements of aerodynamic forces and moments on the vehicle with varying rear wing angle of attack settings. The experiments were performed at a constant wind speed of 40 m/s, equivalent to a Reynolds Number of 4.21×10^6, and were subject to a blockage ratio of approximately 9.6%. The measurements were conducted with an Aerotech® six-component internal balance with a nominal accuracy of ±0.06% of the full scale measurement range, providing an accuracy of ±0.90 N for lift and ±0.18 N for drag.

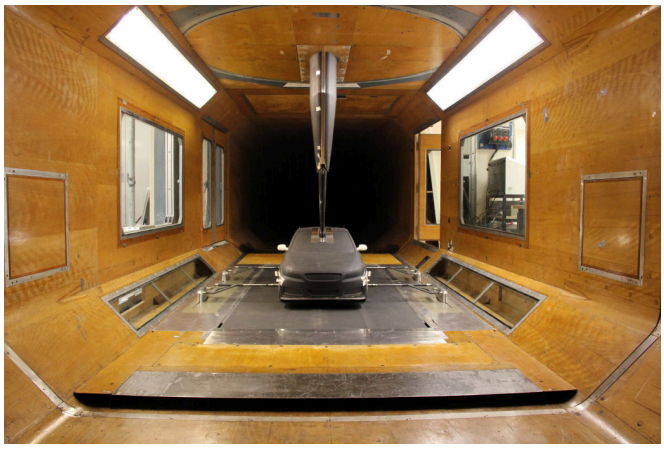


Figure 3: 35% scale *DrivAer hp-F* model in the 8x6 Wind Tunnel using the moving ground setup at Cranfield University. Reproduced from [Rijns, S., Teschner, T.-R., Blackburn, K., Brighton, J., "Effects of cornering conditions on the aerodynamic characteristics of a high-performance vehicle and its rear wing", Physics of Fluids, 36(4), 045119 (2024).], with the permission of AIP Publishing.

Table 1: Main dimensions of the baseline, active concepts, and 35% scale wind tunnel model of the *DrivAer hp-F*

Feature	Baseline	Active	35% scale
Vehicle			
Length (L)	4.6126 m	4.6126 m	1.6144 m
Width	1.7923 m	1.7923 m	0.6273 m
Height	1.3971 m	1.3971 m	0.4890 m
Ride height	0.1300 m	0.1300 m	0.0455 m
Area (A_{ref})	2.1596 m^2	2.1596 m^2	0.2647 m^2
Rear wing			
Chord	0.3143 m	0.3929 m	0.1100 m
Span	1.200 m	1.500 m	0.4200 m

Further details on the wind tunnel experiments are available in our previous work (Rijns et al. (2024b)).

2.3. Operating Conditions

A variety of cornering conditions are considered for the performance analyses to formulate a comprehensive understanding of the potential benefits and limitations of AALB provided by the active aerodynamic devices of the two high-performance vehicle concepts. Corners with radii of 15, 30, and 50 car-lengths (L) are selected to cover various driving scenarios, ranging from tight corner to high-speed bends.

As previously presented in Figure 1, an initial performance assessment of the baseline high-performance vehicle is used to determine representative operating conditions for the CFD simulations on the active high-performance vehicle concepts in each cornering condition. Following the assessment in section 3.1, the 15L, 30L, and 50L radius corners are simulated at 29 m/s, 42 m/s and 54 m/s, respectively.

2.4. Computational Fluid Dynamics

Aerodynamic data for the active high-performance vehicle concepts in the specified operating conditions is obtained through CFD simulations. The methodology builds upon a previously validated approach, which has been extensively employed for aerodynamic research on the *DrivAer hp-F* model across various operating conditions (Rijns et al. (2023), Rijns et al. (2024a), Rijns et al. (2024b), Rijns et al. (2024d)).

2.4.1. Computational Domain & Boundary Conditions

The steady-state cornering conditions are simulated by using a rectangular domain with modified inlet and outlet positions, adopted from our previous work (Rijns et al. (2024b)). The computational domain, illustrated in Figure 4, in combination with a moving reference frame, allows the simulation of various corner radii. This approach eliminates the need for re-meshing the entire domain for each operating condition, thereby improving the numerical workflow efficiency.

The dimensions of the domain follow best practice guidelines for automotive aerodynamic simulations (Lanfrit (2005)), with the domain extending 3L in front, 5L behind, 1.5L above, and 1.5L on either side of the vehicle.

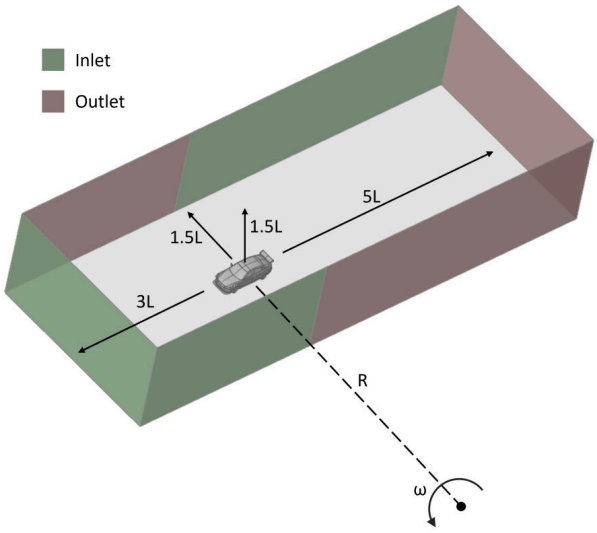


Figure 4: Computational domain with cornering boundary conditions. Reproduced from [Rijns, S., Teschner, T.-R., Blackburn, K., Brighton, J., "Effects of cornering conditions on the aerodynamic characteristics of a high-performance vehicle and its rear wing", Physics of Fluids, 36(4), 045119 (2024).], with the permission of AIP Publishing.

The moving reference frame approach defines a rotational frame motion about an external point, referred to as the centre of rotation, to simulate the curved path during cornering. Since the domain is prescribed with an angular velocity, the ground plane is modelled to remain stationary. Wheel rotation is simulated with rotational moving wall boundary conditions, which prescribe an angular velocity to match the required tangential velocity at each wheel.

As elaborated in section 2.3, representative operating states are selected based on an initial performance assessment of the baseline *DrivAer hp-F*. Furthermore, turbulence conditions are derived from on-road turbulence measurements for ground vehicles, as reported by Saunders and Mansour (2000), to replicate realistic driving conditions. An overview of the simulation settings for each operating condition is provided in Table 2.

2.4.2. Mesh

The computational domain is constructed using an overset mesh approach, which utilises individual unstructured polyhexcore meshes created in ANSYS Fluent Meshing. The overset mesh technique applies data interpolation within overlaying mesh regions, thereby allowing specific component mesh transformations without needing to re-mesh the entire domain. Together with its demonstrated effectiveness in prior studies (Rijns et al. (2024b), Szudarek and Piechna (2021)), the overset mesh methodology is a particularly beneficial approach to improve the workflow efficiency for the substantial amount of CFD simulations in this study.

The overset interfaces of the component meshes are depicted

Table 2: CFD simulation settings for each steady-state cornering operating condition

Feature	**15L**	**30L**	**50L**
Velocity (tangential)	v = 29 m/s	v = 42 m/s	v = 54 m/s
Moving reference frame			
frame motion	rotational	rotational	rotational
motion axis (x, y, z)	0, 0, 1	0, 0, 1	0, 0, 1
velocity	ω = 0.4191 rad/s	ω = 0.3035 rad/s	ω = 0.2341 rad/s
Inlets & Outlets			
velocity-inlet	v = 0 m/s	v = 0 m/s	v = 0 m/s
pressure-outlet	P_{gauge} = 0 Pa	P_{gauge} = 0 Pa	P_{gauge} = 0 Pa
turbulent intensity	I_T = 4%	I_T = 4%	I_T = 4%
turbulent length scale	l_T = 2.5 m	l_T = 2.5 m	l_T = 2.5 m
Wheels			
steering angle	δ = 2.2°	δ = 1.5°	δ = 1.1°
rotation axis			
front (x, y, z)	sin(δ), -1, 0	sin(δ), -1, 0	sin(δ), -1, 0
rear (x, y, z)	0, -1, 0	0, -1, 0	0, -1, 0
velocity			
front inboard	ω = 91.272 rad/s	ω = 132.903 rad/s	ω = 171.225 rad/s
front outboard	ω = 93.299 rad/s	ω = 134.371 rad/s	ω = 172.358 rad/s
rear inboard	ω = 91.267 rad/s	ω = 132.901 rad/s	ω = 171.225 rad/s
rear outboard	ω = 93.294 rad/s	ω = 134.370 rad/s	ω = 172.357 rad/s
Air properties			
reference density	ρ_{ref} = 1.204 kg/m^3	ρ_{ref} = 1.204 kg/m^3	ρ_{ref} = 1.204 kg/m^3
reference dynamic viscosity	μ_{ref} = 1.813e^{-5} kg/(m s)	μ_{ref} = 1.813e^{-5} kg/(m s)	μ_{ref} = 1.813e^{-5} kg/(m s)
reference temperature	T = 293 K	T = 293 K	T = 293 K

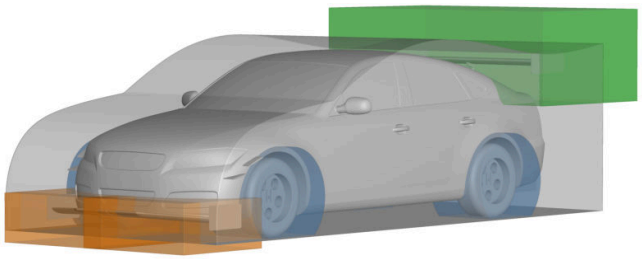


Figure 5: Overset interfaces of the component meshes

in Figure 5, where the interfaces of the vehicle body, front wing elements, and individual wheels are shown in grey, orange and blue, respectively. The tilted rear wing consists a single component mesh, depicted in green, while the split rear wing elements comprise of two individual component meshes. These meshes, superimposed on the background mesh inclusive of refinement zones, form the complete domain. Utilising this approach enables independent adjustments of the wheels' steering angles and operating settings of the active aerodynamics devices.

The mesh settings in this study are derived from our preceding research on the *DrivAer hp-F* model, which evaluated grid convergence and near-wall modelling approaches for cost-effective RANS simulations against experimental data and high-fidelity Delayed Detached Eddy Simulations (DDES) on a wall-resolved mesh with $y^+ < 1$ (Rijns et al. (2024a)).

Accordingly, the base element and vehicle surface element sizes are approximately 7.25% and 0.45% of the vehicle's length, respectively. Element sizes on aerodynamic devices are locally reduced to about 2.5% of the vehicle's length and on small geometric features to about 0.25%. Furthermore, a medium near-wall treatment with a $y^+ \approx$ 120-150 and 4-6 inflation layers is targeted for each operating condition. Additional refinement zones for improved resolution in the vehicle's near-field and wake region are added as well, as depicted in Figure 6.

Altogether, the meshes for the split rear wing concept have an average cell count of approximately 19.6 million, and the meshes for the tilted rear wing concept of around 23.9 million. All meshes generally contain an orthogonal quality above 0.7 for 99% of the cells.

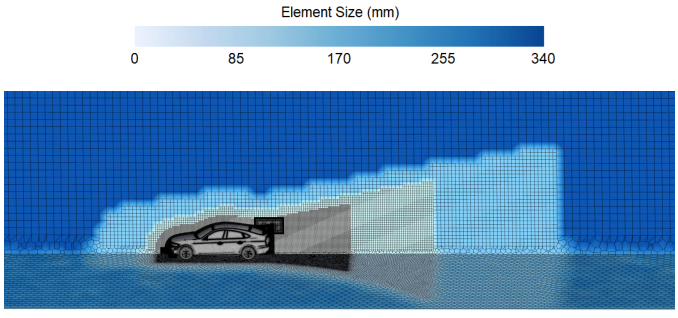


Figure 6: Element sizes in proximity of the vehicle using a slice at y = 0 mm (symmetry) for illustration

2.4.3. Solve

RANS-based CFD simulations are performed using the k-ω SST turbulence model (Menter (1994)) with standard settings in ANSYS Fluent. The selection of the k-ω SST model is based on its demonstrated effectiveness for aerodynamic simulations on the *DrivAer hp-F* model, as evidenced in our prior study which evaluated the accuracy of various RANS models against experimental data and high-fidelity DDES simulations (Rijns et al. (2024a)).

The continuity, momentum, and transport equations for the turbulent kinetic energy and specific dissipation rate are solved. The coupled scheme is deployed for the pressure-velocity coupling and the second order upwind scheme for the spatial discretisation.

During the simulations, lift and drag coefficients were monitored to assess convergence. The settling point of the moving mean of these monitored quantities was typically reached within 200 iterations. Accordingly, the simulations were conducted for a total of 750 iterations, with averaged quantities collected of the last 450 iterations.

The simulations were executed on two nodes consisting of AMD EPYC 7543 processors, utilising a total of 128 cores. The average computational time was approximately 4 hours for the split rear wing concept, and around 5 hours for the tilted rear wing concept.

2.4.4. Data

The aerodynamic analyses in the paper use non-dimensional coefficients of forces and pressures obtained from the CFD simulations. Force coefficients are expressed by Eq. (1), where F_i [N] denotes the numerical force results, C_i [-] the non-dimensional force coefficients, and i is used to indicate lift (L) or drag (D). Similarly, pressure coefficients are given by Eq. (2), where P_s [Pa] represents the numerical static pressure results and C_p [-] the non-dimensional pressure coefficient. Reference quantities of the air density ρ_ref [kg/m^3], freestream velocity v_ref [m/s], and frontal area A_ref [m^2] are listed in Tables 1 and 2.

$$C_\mathrm{i} = \frac{F_\mathrm{i}}{\frac{1}{2}\rho_\mathrm{ref} v_\mathrm{ref}^2 A_\mathrm{ref}} \tag{1}$$

$$C_\mathrm{p} = \frac{P_\mathrm{s} - P_\mathrm{op}}{\frac{1}{2}\rho_\mathrm{ref} v_\mathrm{ref}^2} \tag{2}$$

2.5. Vehicle Dynamics

This research utilises a vehicle dynamics model which incorporates aerodynamic forces, lateral load transfer, and non-linear tyre characteristics to evaluate vehicle performance in steady-state cornering conditions. A general overview of the model, illustrated in Figure 7, is first provided to support the interpretation of detailed formulations discussed later.

The model operates iteratively, cycling through velocities for a specified corner radius. At each velocity, the required lateral force for the vehicle to maintain its cornering trajectory is calculated for both the front and rear axles. To ensure that aerodynamic performance is accurately represented, aerodynamic

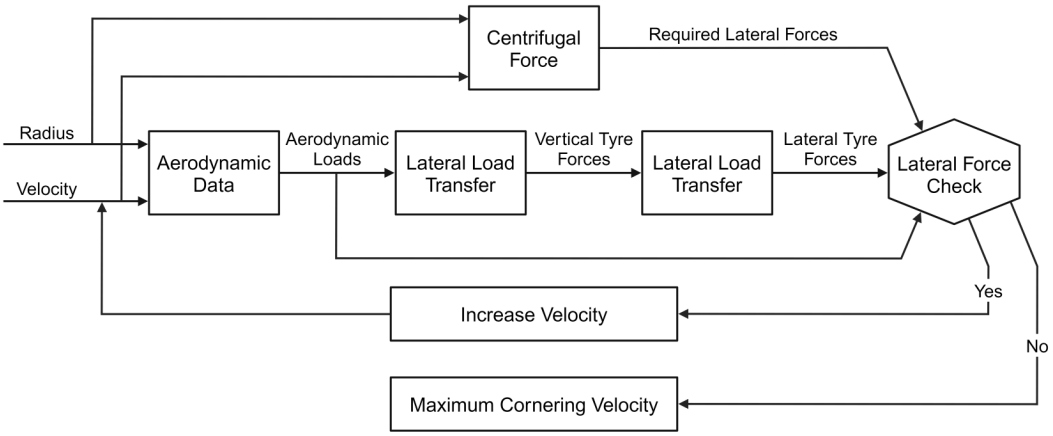


Figure 7: Vehicle dynamics model procedure

maps are created for the specified cornering conditions and incorporated into the model. These maps, combined with the effects of lateral load transfer, are used to calculate the vertical forces acting on each tyre.

These vertical forces are then input into the tyre model, which iterates through front and rear slip angles until the required lateral force for each axle is achieved. This iterative process continues, with the velocity incrementally increasing until the required lateral force at either the front or rear axle can no longer be produced. The final velocity at this point represents the maximum achievable velocity for the given corner radius.

The model assumes traction-limited states, implying that the vehicle's propulsion system can generate the necessary power to achieve the maximum velocity. The vehicle parameters used in the model, listed in Table 3, are based on indicative specifications of sports and racing cars (Dixon (1996)).

2.5.1. Vehicle System

The vehicle dynamics system is based on a bicycle model, which has been demonstrated to adequately simulate dominant vehicle dynamics effects even in extreme operating conditions (Velenis et al. (2010)), making it a suitable approach for this study.

The vehicle dynamics system, depicted in Figure 8, uses combined slip angles α_f (rad) and α_r (rad) for the front and rear tyres, respectively. Applying a small angle approximation, the steering angle δ (rad) and side slip angle β (rad) are expressed by Eqs. (3) and (4). Small angle approximations employed in this study have a maximum error of approximately 0.2%, which is considered acceptable for the purpose of the analyses.

$$\delta = \frac{l}{R} + \alpha_f - \alpha_r \tag{3}$$

$$\beta = \frac{l_r}{R} - \alpha_r \tag{4}$$

2.5.2. Centrifugal Force

In order for a vehicle to maintain its trajectory in a steady-state cornering condition, it must generate a lateral cornering force equal to the centrifugal force F_c (N), formulated by Eq.(5). Here, m (kg) represents the total vehicle mass, V (m/s) the vehicle's velocity, R (m) the corner radius, and a (m/s^2) the vehicle's lateral acceleration.

$$F_c = m\frac{V^2}{R} = ma \tag{5}$$

The moment equilibrium about the vehicle's centre of gravity (COG) determines the required lateral forces, which must be produced at front $F_{yf,req}$ (N) and rear $F_{yr,req}$ (N) axles to maintain the cornering trajectory, as expressed by Eqs. (6) and (7). In these equations, l (m) denotes the wheelbase length, and l_f (m) and l_r (m) the distances between COG and the front and rear axles, respectively.

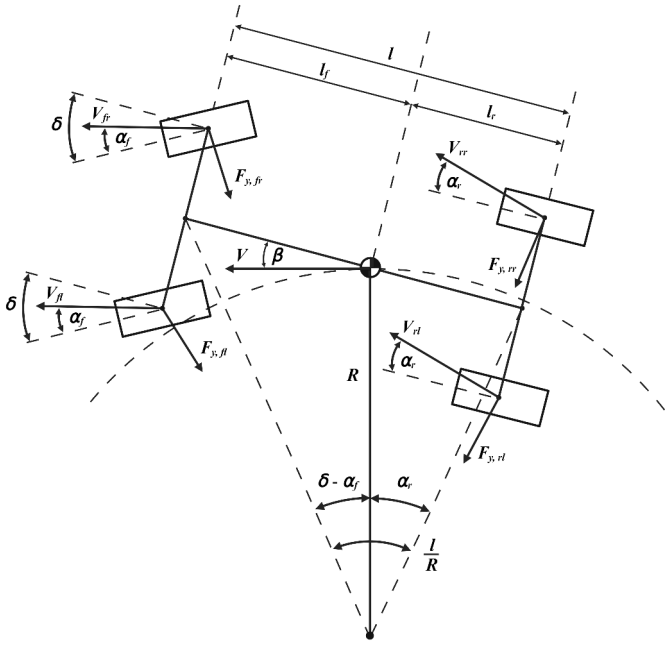


Figure 8: Schematic representation of the vehicle dynamics system

Table 3: Vehicle parameters for the vehicle dynamics model

Parameter	Symbol	Unit	Quantity
Mass			
sprung vehicle body	m_b	kg	1300
driver	m_d	kg	75
front unsprung mass	m_{uf}	kg	90
rear unsprung mass	m_{ur}	kg	100
total sprung mass	m_s	kg	1375
total mass	m	kg	1565
Dimensions			
wheelbase length	l	m	2.786
distance front axle to COG	l_f	m	1.4766
distance front axle to COG	l_r	m	1.3094
height COG	h_{COG}	m	0.5
height front unsprung mass	h_{uf}	m	0.2969
height rear unsprung mass	h_{ur}	m	0.2969
height roll centre at COG position	h	m	0.0912
height front roll centre	h_f	m	0.2969
height rear roll centre	h_r	m	0.2969
distance roll axis to COG	d	m	0.4088
width front track	t_f	m	1.5204
width rear track	t_r	m	1.5204
Suspension			
roll stiffness	k_ϕ	Nm/rad	$1.1459 \cdot 10^5$
front roll stiffness	k_ϕ	Nm/rad	$6.3025 \cdot 10^4$
rear stiffness	k_ϕ	Nm/rad	$5.1566 \cdot 10^4$

$$F_{yf,req} = F_c \frac{l_r}{l} \tag{6}$$

$$F_{yr,req} = F_c \frac{l_f}{l} \tag{7}$$

2.5.3. Vertical wheel load

The actual lateral forces produced by the tyres are dependent on the individual vertical wheels loads. In steady-state cornering, the loads are influenced by aerodynamic forces and lateral load transfer. A schematic view of lateral load transfer during cornering is provided in Figure 9, serving as a visual aid for the subsequent formulations for vertical wheel loads.

The front and rear static wheel loads, denoted with W_f (N) and W_r (N), are defined by Eqs. (8) and (9). Here, m_s (kg) represents the sprung mass, m_{uf} (kg) the front unsprung mass, m_{ur} (kg) the rear unsprung mass, and g (m/s^2) the gravitational acceleration.

$$W_f = \frac{1}{2} g (m_{uf} + m_s \frac{l_r}{l}) \tag{8}$$

$$W_r = \frac{1}{2} g (m_{ur} + m_s \frac{l_f}{l}) \tag{9}$$

The lateral load transfers resulting from the centrifugal force on the front and rear unsprung masses, indicated with $F_{Tf,1}$ (N) and $F_{Tr,2}$ (N) respectively, are expressed by Eqs. (10) and (11). In these equations, h_{uf} (m) and h_{ur} (m) denote the heights of the front and rear unsprung masses, and t_f (m) and t_r (m) the front and rear track widths.

$$F_{Tf,1} = m_{uf} a \left(\frac{h_{uf}}{t_f} \right) \tag{10}$$

$$F_{Tr,1} = m_{ur} a \left(\frac{h_{ur}}{t_r} \right) \tag{11}$$

The centrifugal force on the sprung mass can be expressed as a force acting on the roll axis, transmitted via the suspension

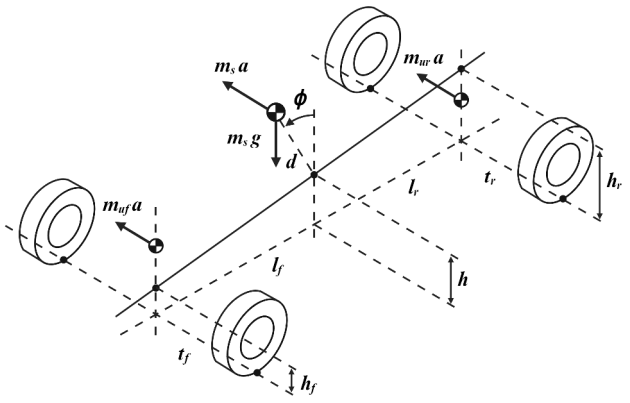


Figure 9: Schematic representation of lateral load transfer

links, and an additional roll couple due to the distance between the COG and the roll axis, transmitted through the springs. Similarly, the aerodynamic loads on the sprung mass can be conceptualised as an aerodynamic side force acting on the roll axis, and an aerodynamic roll moment about the roll axis.

Considering the forces transmitted through the suspension links first, the load transfer resulting from the centrifugal is distributed between the front and rear axles by the position of the vehicle's COG. The magnitudes of the aerodynamic side force components acting on the front and rear roll centres, represented by F_{Sf} (N) and F_{Sr} (N), impact the lateral load transfer resulting from aerodynamic loads at the respective axles. Together, the forces transmitted via the suspension links induce a lateral load transfer at the front and rear axle, denoted by $F_{Tf,2}$ (N) and $F_{Tr,2}$ (N), which are formulated by Eqs. (12) and (13). Here, h_f (m) and h_r (m) represent the front and rear roll centre heights, and the aerodynamic side force components are defined in the same direction as the centrifugal force.

$$F_{Tf,2} = m_s a \left(\frac{l_r}{l}\right)\left(\frac{h_f}{t_f}\right) + F_{Sf}\left(\frac{h_f}{t_f}\right) \tag{12}$$

$$F_{Tr,2} = m_s a \left(\frac{l_f}{l}\right)\left(\frac{h_r}{t_r}\right) + F_{Sr}\left(\frac{h_r}{t_r}\right) \tag{13}$$

The roll moment of the sprung mass about the vehicle's roll axis, generated by the centrifugal force and aerodynamic loads, is transmitted through the suspension springs. By applying a small angle approximation, the resultant roll angle of the sprung mass ϕ (rad) is expressed by Eq. (14). Here, $M_{A,rc}$ (Nm) denotes the aerodynamic roll moment about the vehicle's roll centre at the COG position, defined in the opposite direction of the moment created by the centrifugal force. The distance between the COG and the roll axis is represented by d (m), and the total roll stiffness by k_ϕ (Nm/rad).

$$\phi = \frac{m_s a d - M_{A,rc}}{k_\phi - m_s g d} \tag{14}$$

The roll moments reacted at front and rear axles, denoted by M_f (Nm) and M_r (Nm), are proportional to the roll stiffnesses of the axles. The roll moments are formulated by Eqs. (15) and (16), where the roll stiffnesses of the front and rear axles are represented by $k_{\phi f}$ (Nm/rad) and $k_{\phi r}$ (Nm/rad), respectively.

$$M_f = k_{\phi f}\phi \tag{15}$$

$$M_r = k_{\phi r}\phi \tag{16}$$

The lateral load transfers at the front $F_{Tf,3}$ and rear $F_{Tf,3}$ axles, resulting from the roll moments, are subsequently expressed by Eqs. (10) and (11).

$$F_{Tf,3} = \frac{M_f}{t_f} \tag{17}$$

$$F_{Tr,3} = \frac{M_r}{t_r} \tag{18}$$

During cornering, lateral load transfer occurs from the inside to the outside wheels. Given that this study considers left-hand corners, the load transfers from the left to the right tyres. Additionally, vertical wheel loads are affected by aerodynamic downforce on each wheel, as formulated by Eqs. (19)-(22). The downforce on the front left, front right, rear left, and rear right tyres is denoted by $F_{DF,fl}$ (N), $F_{DF,fr}$ (N), $F_{DF,rl}$ (N), and $F_{DF,rr}$ (N). The overall vertical forces acting on the respective tyres are represented by $F_{Z,fl}$ (N), $F_{Z,fr}$ (N), $F_{Z,rl}$ (N), and $F_{Z,rr}$ (N).

$$F_{Z,fl} = W_f - F_{Tf,1} - F_{Tf,2} - F_{Tf,3} + F_{DF,fl} \tag{19}$$

$$F_{Z,fr} = W_f + F_{Tf,1} + F_{Tf,2} + F_{Tf,3} + F_{DF,fr} \tag{20}$$

$$F_{Z,rl} = W_r - F_{Tr,1} - F_{Tr,2} - F_{Tr,3} + F_{DF,rl} \tag{21}$$

$$F_{Z,rr} = W_r + F_{Tr,1} + F_{Tr,2} + F_{Tr,3} + F_{DF,rr} \tag{22}$$

2.5.4. Tyre Model

The actual lateral force produced by each individual tyre is modelled as a function of slip angle and vertical load, using the widely deployed Pacejka '96 model (Pacejka (2012)). The lateral tyre force F_y (N) is described by Eq. (23), where α_i (rad) is the slip angle, with subscript i indicating the front (f) or rear (r) slip angle.

$$F_y = D_y \sin[C_y \tan^{-1}\{B_y\alpha_i - E_y(B_y\alpha_i - \tan^{-1}(B_y\alpha_i))\}] \tag{23}$$

The peak value D_y, shape factor C_y, curvature factor E_y, stiffness factor B_y, and normalised change in vertical load $\mathrm{d}f_Z$ are described by Eqs. (24)-(28). Here, the nominal vertical wheel load is denoted by F_{Z0} (N), the actual vertical wheel load by F_Z (N), and the wheel camber by γ (rad). Furthermore, The Pacejka coefficients are represented by $\mathrm{p}_{CY1}...\mathrm{p}_{VY4}$ and the scaling factors by $\lambda_{\mu y}...\lambda_{Ey}$.

$$D_y = F_Z(\mathrm{p}_{DY1} + \mathrm{p}_{DY2}\mathrm{d}f_Z)(1 - \mathrm{p}_{DY3}\gamma^2)\lambda_{\mu y} \tag{24}$$

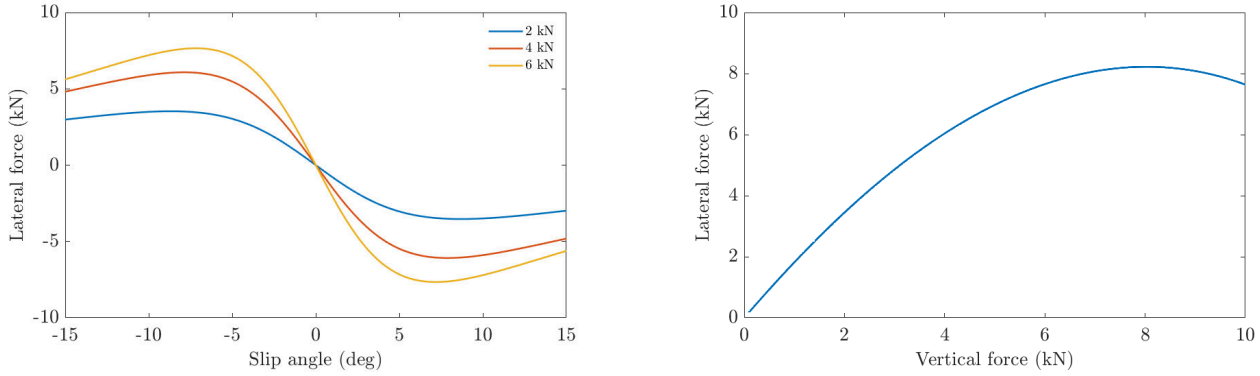
$$C_y = \mathrm{p}_{CY1}\lambda_{Cy} \tag{25}$$

$$B_y = \frac{\mathrm{p}_{KY1}F_{Z0}\sin\left[2\tan^{-1}\left(\frac{F_Z}{\mathrm{p}_{KY2}F_{Z0}\lambda_{Z0}}\right)\right](1 - \mathrm{p}_{KY3}|\gamma|)\lambda_{FZ0}\lambda_{Kya}}{C_y D_y} \tag{26}$$

$$E_y = (\mathrm{p}_{EY1} + \mathrm{p}_{EY2}\mathrm{d}f_Z)(1 - (\mathrm{p}_{EY3} + \mathrm{p}_{EY4}\gamma)\mathrm{sgn}(\alpha_i))\lambda_{Ey} \tag{27}$$

$$\mathrm{d}f_Z = \frac{F_Z - F_{Z0}}{F_{Z0}} \tag{28}$$

Following the procedure from (Seward (2014)), Pacejka coefficients are derived which approximate lateral tyre force data for a 250/570R13 Avon British F3 tyre with 0° camber (Avon



(a) (b)

Figure 10: (a) Lateral tyre force as a function of slip angle, and (b) lateral tyre force as a function of vertical force at a constant slip angle of α = -7°

Tyres (2024)). The tyre model coefficients are listed in Table 4, and the corresponding lateral tyre force characteristics are illustrated in Figure 10.

Figure 10a reveals that the lateral tyre force initially increases almost linearly with small slip angles, but the relationship becomes non-linear near the tyre's peak grip, after which lateral force reduces with slip angle. Additionally, the diminishing gain in lateral force with constant vertical load increments indicates grip saturation at high vertical loads. This vertical load sensitivity is especially evident when the lateral tyre force is expressed as a function of the vertical tyre force at a constant slip angle, as presented in Figure 10b. Due to this non-linear relation, an unbalanced vertical load across an axle will reduce the potential total lateral force production from that axle.

Table 4: Coefficients for the lateral tyre force model

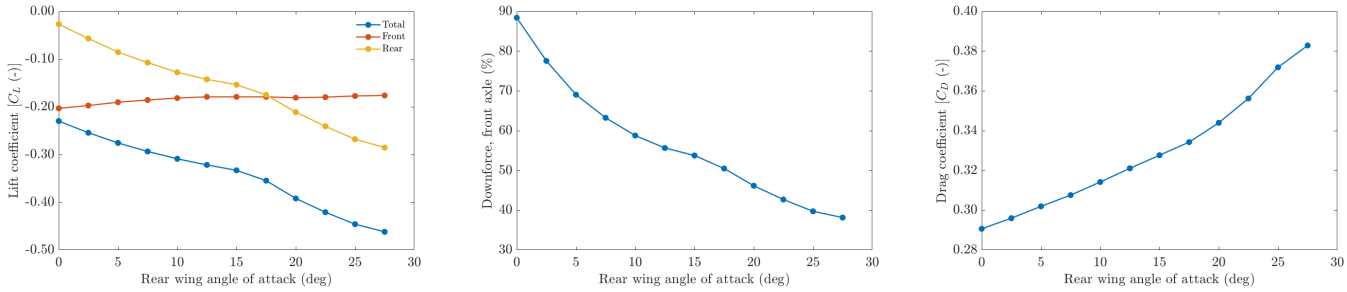
Coefficient	Value	Coefficient	Value
F_{Z0} (N)	4905	p_{KY1}	-35
p_{CY1}	2.5	p_{KY2}	3
p_{DY1}	-1.41	p_{KY3}	0
p_{DY2}	0.6	$\lambda_{\mu y}$	1
p_{DY3}	0	λ_{Cy}	1
p_{EY1}	0.5	λ_{FZ0}	1
p_{EY2}	0	λ_{Kya}	1
p_{EY3}	0	λ_{Ey}	1
p_{EY4}	0	γ (°)	0

3. Results & Discussions

The performance of the baseline *DrivAer hp-F* configuration is first examined to establish a foundation for subsequent analyses. As previously detailed in section 2, the results of this evaluation are utilised for formulating the operating states for the CFD simulations on the active high-performance vehicle concepts. Following the baseline performance assessment, the influence of AALB on the cornering performance of the split rear wing and tilted rear wing concepts is discussed. Finally, the AALB capability of the split rear wing and tilted rear wing concepts is compared.

3.1. Baseline Vehicle Configuration

The experimental force data for the baseline *DrivAer hp-F*, presented in Figure 11, shows two downforce enhancements regions across the rear wing's angle of attack range. In the initial 0°-15° range, downforces increases by approximately $\Delta C_L \approx -0.103$ until the rear wing stalls at around 15°. Beyond the stall angle, downforce increases by another $\Delta C_L \approx -0.129$ along the 15°-27.5° range.



(a) (b) (c)

Figure 11: Wind tunnel measurement results of (a) lift coefficients, (b) downforce distribution, and (c) drag coefficients for the baseline *DrivAer hp-F* with varying rear wing angle of attack

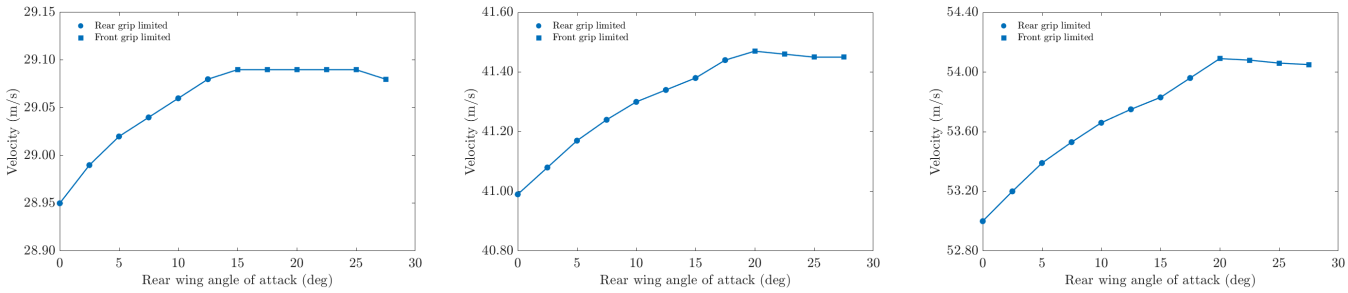


Figure 12: Maximum cornering velocity for the baseline *DrivAer hp-F* in the (a) 15L radius corner, (b) 30L radius corner, and (c) 50L radius corner operating conditions. The marker style indicates front or rear grip limit behaviour.

Prior analyses have shown that downforce generation from the rear wing itself diminishes after its stall angle, but high angles of attack create substantial upstream pressurisation, reducing lift generation along the vehicle's upper surfaces (Rijns et al. (2024b,d)). However, high rear wing angles of attack also produce substantially more drag. The average drag penalty per 2.5° angle of attack increment rises by nearly 80%, from $\Delta C_D \approx 0.006$ in the 0°-15° range to $\Delta C_D \approx -0.011$ in the 15°-27.5° range.

The downforce produced by the rear wing primarily acts on the rear axle, while slightly reducing front axle downforce by $\Delta C_L \approx 0.027$ across the 0°-27.5° range. Consequently, the vehicle's aerodynamic balance shifts from around 88% front axle downforce at 0° to approximately 38% at 27.5°.

Performance results using this aerodynamic data, illustrated in Figure 12, the maximum velocity in each cornering condition initially increases with the rear wing's angle of attack, before peaking and declining. Relative to the performance with a 0° rear wing angle of attack, the maximum cornering velocity increases by approximately $\Delta v \approx 0.14$ m/s (0.5%) at 15° in the 15L radius corner, $\Delta v \approx 0.48$ m/s (1.2%) at 20° in the 30L radius corner, and $\Delta v \approx 1.09$ m/s (2.1%) at 20° in the 50L radius corner.

Notably, peak performance across the cornering conditions is achieved at front axle downforce distributions ranging from approximately 45% to 55%. Furthermore, it is evident that the rear wing's impact on the vehicle's cornering performance becomes more substantial at higher velocities. This is a result of the absolute magnitude of aerodynamic downforce, which quadratically increases with the vehicle's velocity. Figure 12 also shows that the vehicle's performance is initially limited by the grip generated by the rear tyres, transitioning to being front grip limited at higher rear wing angles of attack.

To further elaborate on the vehicle's limit behaviour, the lateral tyre forces for front and rear grip limited states in the 50L radius corner are presented in Figure 13. It has been demonstrated that front axle downforce slightly diminishes with rear wing angles of attack, whereas rear axle downforce noticeably enhances. The reduced front axle downforce together with the increased lateral load transfer at a 20° rear wing angle of attack cause a reduction in the potential grip production of the front inside tyre compared to at a 0° rear wing angle of attack. Conversely, despite the larger lateral load transfer, the enhanced rear axle downforce at the 20° rear wing angle of attack improves the potential grip production of both the rear inside and outside tyres.

Consequently, the combined lateral tyre forces, depicted in 13c and 13d, demonstrate that if the velocity of the vehicle

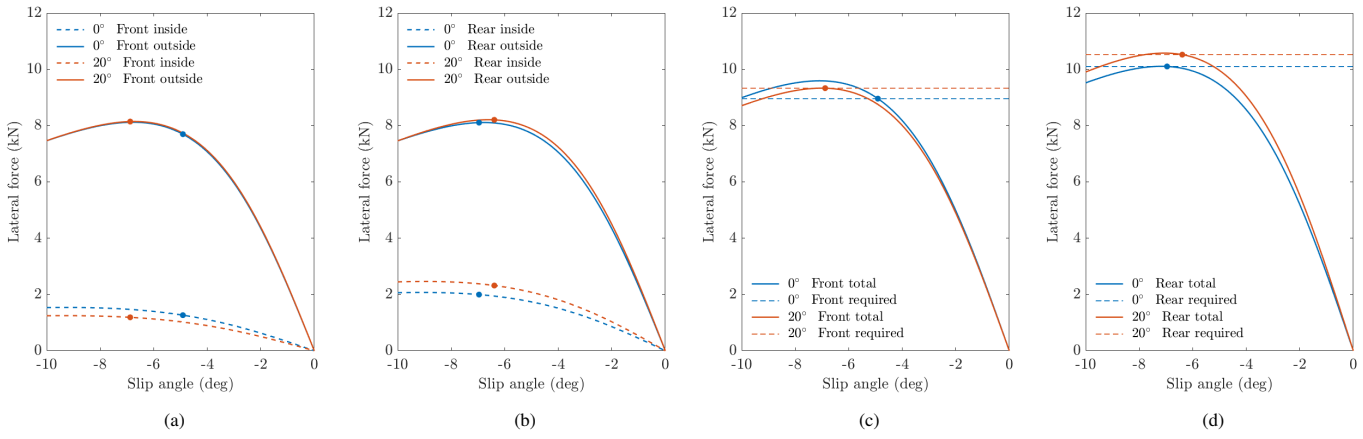


Figure 13: Comparison between the lateral forces produced by the (a) front tyres, (b) rear tyres, (c) front tyres combined, and (d) rear tyres combined of the baseline *DrivAer hp-F* with 0° and 20° rear wing angles of attack in the 50L radius corner

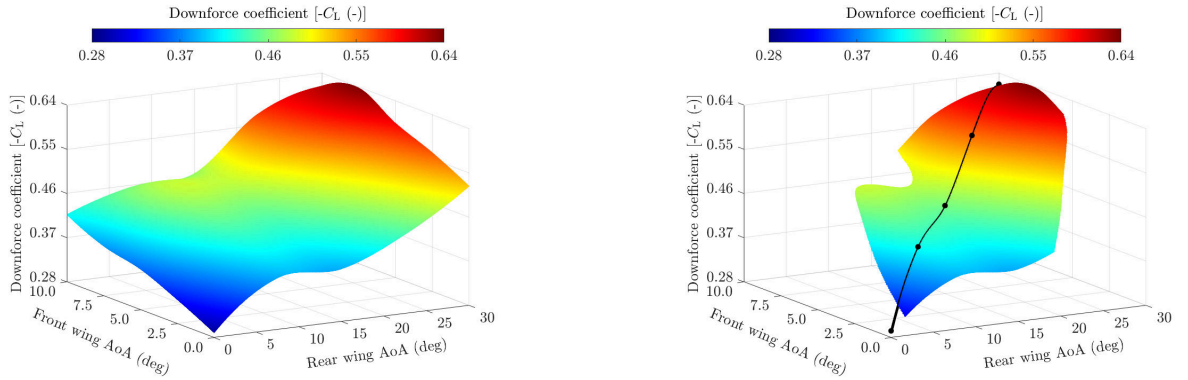


Figure 14: (a) Downforce coefficients on the vehicle body for the full range of simulated front and rear wing angles of attack, and (b) downforce coefficients on the vehicle body in the 40%-60% front axle downforce distribution region, including the determined operating line and settings utilised for the control strategy

with a 0° rear wing angle of attack continues to increase, the rear tyres would not be able generate the required lateral force, leading to oversteering limit behaviour. Contrarily, at a 20° rear wing angle of attack, the front tyres would produce an insufficient lateral force, resulting in understeering limit behaviour. Additionally, both figures indicate that the rear axle must generate a larger lateral force to maintain the moment equilibrium about the vehicle's COG, given that the COG is positioned closer to the rear axle.

3.2. Active Aerodynamic Load Balancing

The split rear wing and tilted rear wing high-performance vehicle concepts, detailed in Section 2.1, are designed to manipulate the distribution of aerodynamic loads to improve cornering performance. This section first discusses the control strategy developed for the active aerodynamic devices on these high-performance vehicle concepts, followed by analyses of the aerodynamic characteristics and cornering performances. The section concludes with a comparison between the AALB capabilities of both high-performance vehicle concepts.

3.2.1. Control Strategy

The control strategy in the present study is designed to operate the active aerodynamic devices of both high-performance vehicle concepts at comparable operating settings to ensure a consistent comparison between both concepts. The control strategy leverages findings from the initial performance assessment of the baseline vehicle, which demonstrated that a balanced front-to-rear downforce distribution is essential for achieving high cornering velocities. The settings for the front and rear located active aerodynamic devices are therefore coupled on either side of the high-performance vehicle concepts to maintain this balance.

The operating settings are derived from aerodynamic data obtained by varying the front and rear wing angles of attack under straight-line conditions, depicted in Figure 14a. A viable operating space of front and rear wing angle of attack combinations is determined using a 40%-60% front axle downforce distribution constraint, illustrated in Figure 14b. Within the defined space, this study opted to use an operating line representing linear combinations of front and rear wing angles of attack, sampled at five evenly spaced operating settings that are simulated to map the aerodynamic performance of the high-performance vehicle concepts.

Accordingly, operating settings for the split rear wing concept pair a 2.5° front wing element angle of attack increment with a 7.5° rear wing element angle of attack increment on the same side of the vehicle, as detailed in Tables 5 and 6. To establish comparable operating settings for the tilted rear wing concept, a 2.5° front wing element angle of attack increment is coupled with a 3.75° rear wing angle of attack increment and 3° upward tilt of the rear wing on the same side of the vehicle, as outlined in Tables 5 and 7.

Table 5: Split front wing: angles of attack for the inside (α_I) and outside (α_O) located elements for each operating setting combination

	O1	O2	O3	O4	O5
	α_I | α_O	α_I | α_O	α_I | α_O	α_I | α_O	α_I | α_O
I1	0° | 0°	0° | 2.5°	0° | 5°	0° | 7.5°	0° | 10°
I2	2.5° | 0°	2.5° | 2.5°	2.5° | 5°	2.5° | 7.5°	2.5° | 10°
I3	5° | 0°	5° | 2.5°	5° | 5°	5° | 7.5°	5° | 10°
I4	7.5° | 0°	7.5° | 2.5°	7.5° | 5°	7.5° | 7.5°	7.5° | 10°
I5	10° | 0°	10° | 2.5°	10° | 5°	10° | 7.5°	10° | 10°

Table 6: Split rear wing: angles of attack for the inside (α_I) and outside (α_O) located elements for each operating setting combination

	O1		O2		O3		O4		O5	
	α_I	α_O	α_I	α_O	α_I	α_O	α_I	α_O	α_I	α_O
I1	0°	0°	0°	7.5°	0°	15°	0°	22.5°	0°	30°
I2	7.5°	0°	7.5°	7.5°	7.5°	15°	7.5°	22.5°	7.5°	30°
I3	15°	0°	15°	7.5°	15°	15°	15°	22.5°	15°	30°
I4	22.5°	0°	22.5°	7.5°	22.5°	15°	22.5°	22.5°	22.5°	30°
I5	30°	0°	30°	7.5°	30°	15°	30°	22.5°	30°	30°

Table 7: Tilted rear wing: angles of attack (α_A) and tilt angles (α_T) for each operating setting combination

	O1		O2		O3		O4		O5	
	α_A	α_T	α_A	α_T	α_A	α_T	α_A	α_T	α_A	α_T
I1	0°	0°	3.75°	3°	7.5°	6°	11.25°	9°	15°	12°
I2	3.75°	-3°	7.5°	0°	11.25°	3°	15°	6°	18.75°	9°
I3	7.5°	-6°	11.25°	-3°	15°	0°	18.75°	3°	22.5°	6°
I4	11.25°	-9°	15°	-6°	18.75°	-3°	22.5°	0°	26.25°	3°
I5	15°	-12°	18.75°	-9°	22.5°	-6°	26.25°	-3°	30°	0°

By adjusting the operating settings for the active aerodynamic devices located at the inside and outside of the high-performance vehicle concepts, the distribution of aerodynamics loads across the inside and outside tyres can be influenced. Given that the control strategies for both concepts apply similar operating settings, a consistent comparison between the two concepts can be conducted in terms of their performance and AALB capabilities.

3.3. Split Rear Wing

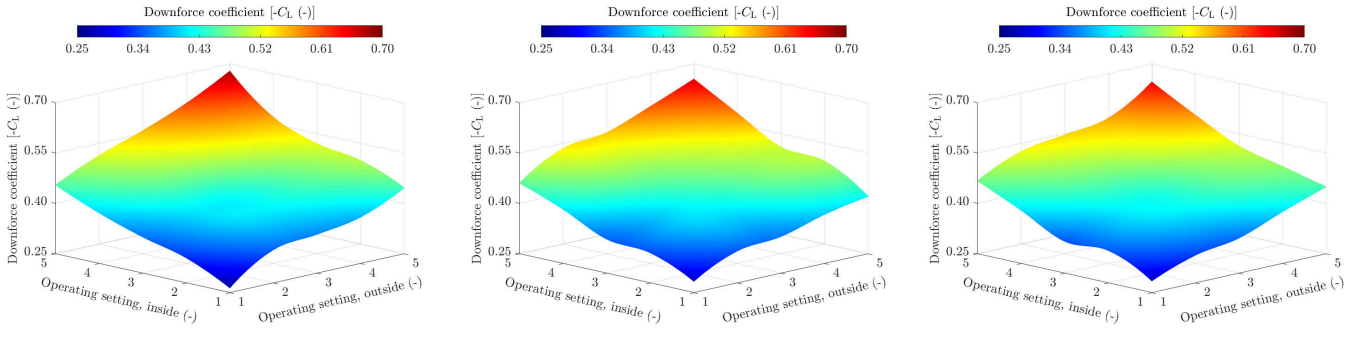
Analyses of the aerodynamic performance of the split rear wing high-performance vehicle concept reveal that downforce and drag coefficients generally increase with higher operating settings for the inside and outside active aerodynamic devices throughout the different cornering conditions, as observed in Figure 15. The rate at which downforce coefficients increase is highest in the 15L radius corner and lowest in the 50L radius corner, indicating the response to operating settings becomes slightly more gradual with increasing corner radii.

Inside dominant operating states mainly exhibit higher downforce and lower drag coefficients than outside dominant operating states. This observations is especially evident in 15L radius corner, suggesting a favourable flow alignment on the inside of the vehicle in tighter corners. The maximum downforce coefficient in the 15L radius corner also exceeds that of the 30L and 50L radius corners by 3.5% and 5%, respectively, whereas the maximum drag coefficient is only 1% higher. Across the operating states, the front axle downforce distribution varies from approximately 49% to 57%, thereby remaining within the intended range of the control strategy.

Figure 16 demonstrates that aerodynamic performance variations between maximum symmetric operating states in different cornering conditions primarily occur on the underbody. Upper body surfaces depict comparable pressure coefficient distributions, where the uniform high-pressure region on top of the split rear wing elements produces a noticeable upstream pressurisation along the roof. On the underbody, the high symmetric front wing settings result in substantial low-pressure regions on both elements. Another pronounced low-pressure area is generated around the front axle, which develops further downstream with reducing corner radii. Flow conditions in tight corners also demonstrate to favour low-pressure generation on the diffuser section on the inside of the vehicle, whereas the pressure coefficient distribution becomes more symmetric with large corners which approximate symmetric straight-line conditions.

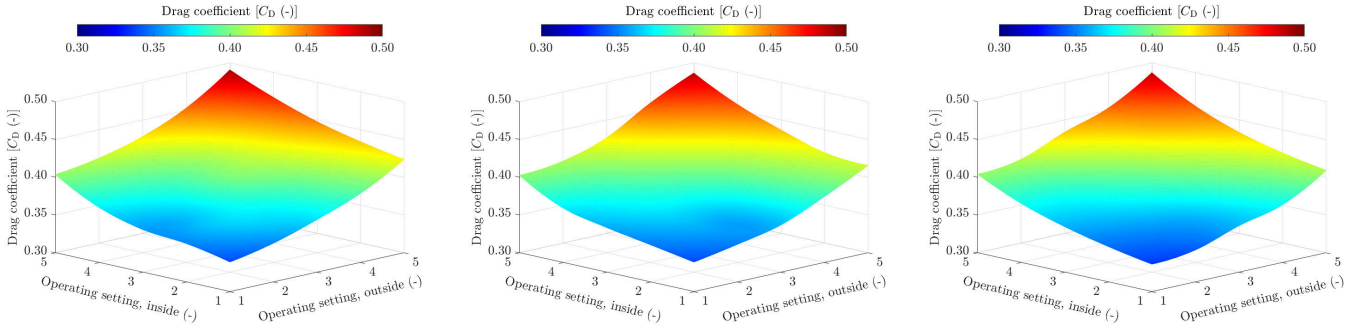
Maximum inside bias operating states generate a more substantial high-pressure region on the upper surface of the inside element than on the outside element of the split rear wing in each cornering condition, as shown in Figure 17. The pressure difference between the split rear wing elements induces a vortex which adversely affects the high-pressure region on the outside element. Furthermore, the upstream pressurisation in this operating state is primarily generated by the inside element, thereby considerably less substantial compared to the maximum symmetric operating state.

The pressure coefficient distributions on the underbody of the vehicle with a maximum inside bias operating state show that the inside element of the split front wing generates a more significant low-pressure region than the outside element. The pressure difference between the front wing elements also drives the formation of a vortex, which propagates along the floor and leaves a low-pressure trace. Additionally, the front wing element settings influence downstream flow conditions, where high angles of attack support low-pressure generation in the dif-



15L 30L 50L

(a)



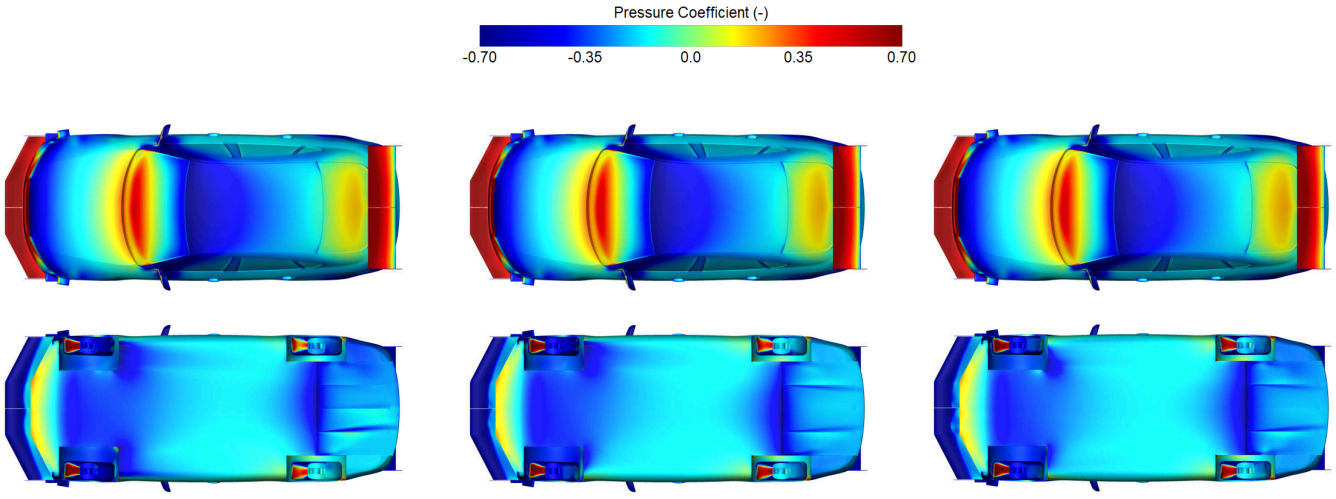
15L 30L 50L

(b)

Figure 15: (a) Downforce coefficients and (b) drag coefficients as a function of the operating settings for the inside and outside located active aerodynamic devices of the split rear wing high-performance vehicle concept in various cornering conditions

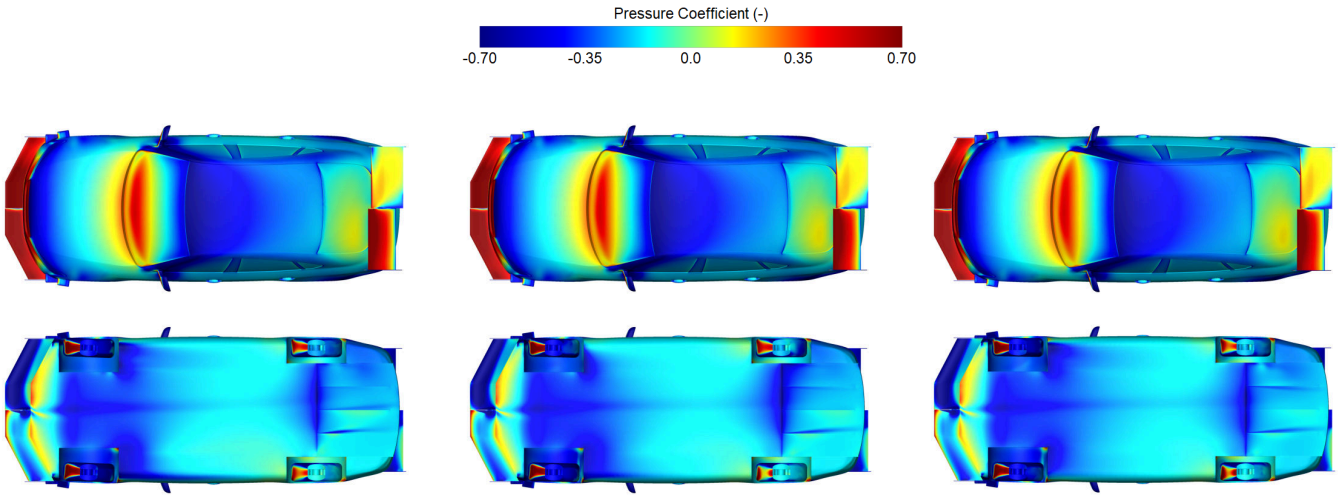
fuser on the same side of the vehicle. This seems especially evident in smaller corners, likely augmented by the effects of flow alignment discussed for the maximum symmetric operating state.

Having established an understanding of the functioning behind the active aerodynamic devices of the split rear wing high-performance vehicle concept, Figure 18 presents the influence of the operating states on the downforce acting on the inside and outside tyres in each cornering condition. As previously identified, flow conditions in tight corners have shown to ben-



(a) (b) (c)

Figure 16: Pressure coefficient distribution on the split rear wing high-performance vehicle concept in its maximum symmetric operating state (5,5) in the (a) 15L radius corner, (b) 30L radius corner, and (c) 50L radius corner

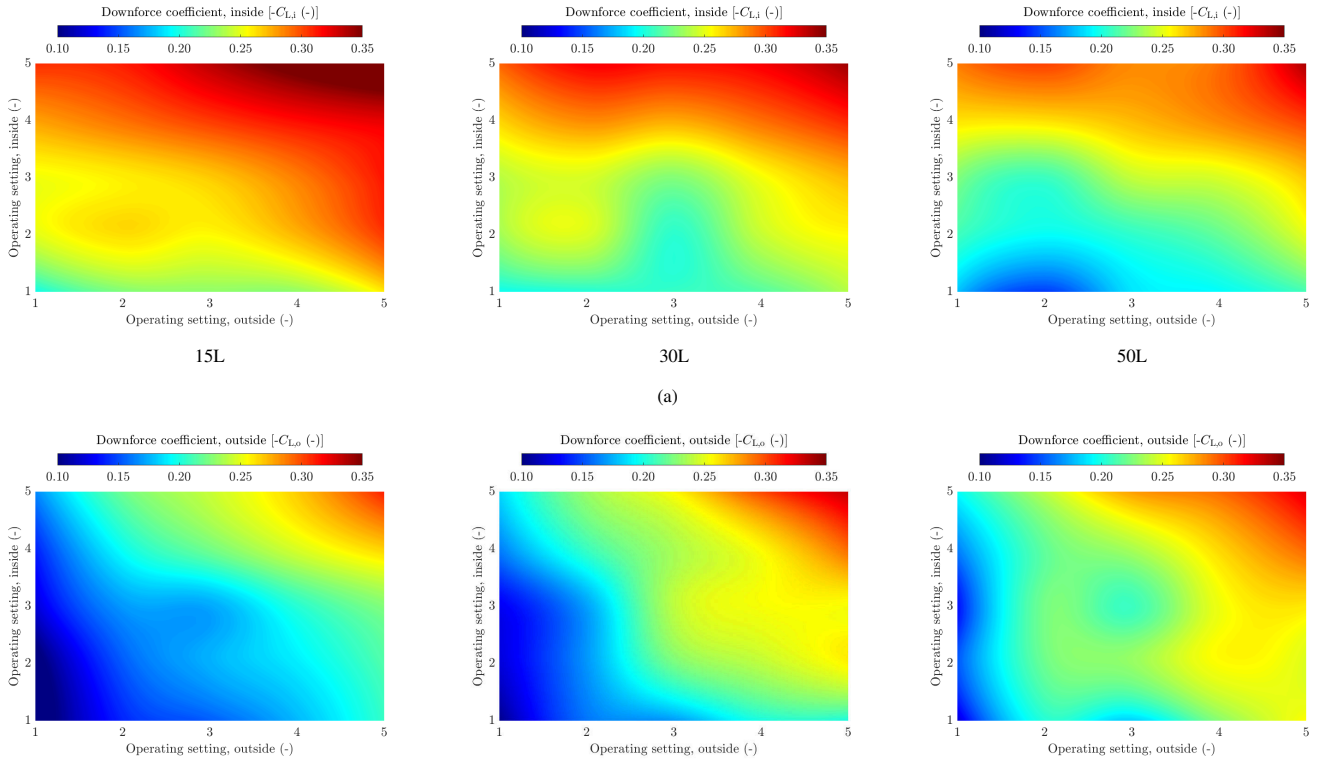


(a) (b) (c)

Figure 17: Pressure coefficient distribution on the split rear wing high-performance vehicle concept in its maximum inside bias operating state (1,5) in the (a) 15L radius corner, (b) 30L radius corner, and (c) 50L radius corner

efit downforce generation on the inside of the vehicle. In accordance, the highest inside and lowest outside downforce coefficients are generally observed in the 15L radius corner. Conversely, the nearly symmetric flow conditions in the 50L radius corner result in more balanced magnitudes of inside and outside downforce coefficients.

Throughout the cornering conditions, the inside downforce coefficients increase with higher operating settings for the aerodynamic devices on the same side of the vehicle. However, for a given inside operating setting, the inside downforce co-



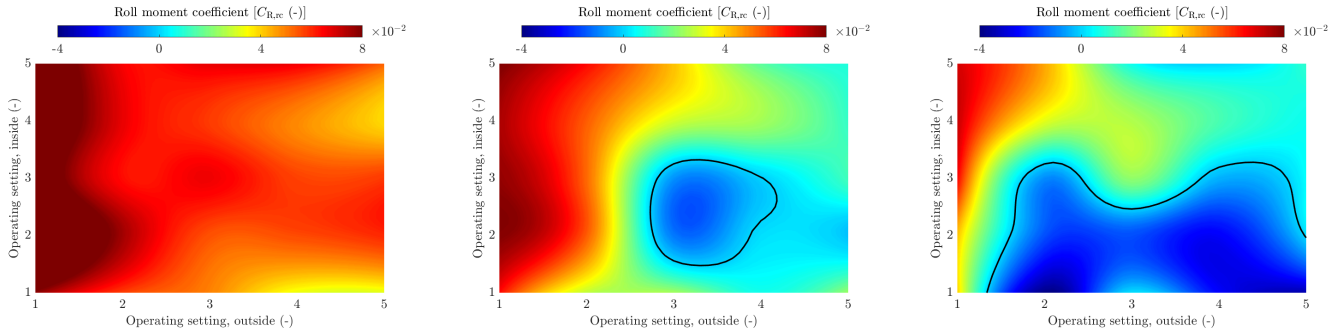
15L 30L 50L

(a)

15L 30L 50L

(b)

Figure 18: Downforce coefficients on the (a) inside tyres and (b) outside tyres as a function of the operating settings for the inside and outside located active aerodynamic devices of the split rear wing high-performance vehicle concept in various cornering conditions



(a) (b) (c)

Figure 19: Aerodynamic roll moment coefficients about the vehicle's roll axis as a function of the operating settings for the inside and outside located active aerodynamic devices of the split rear wing high-performance vehicle concept in the (a) 15L radius corner, (b) 30L radius corner, and (c) 50L radius corner. The black contour lines mark an aerodynamic roll moment coefficient of zero.

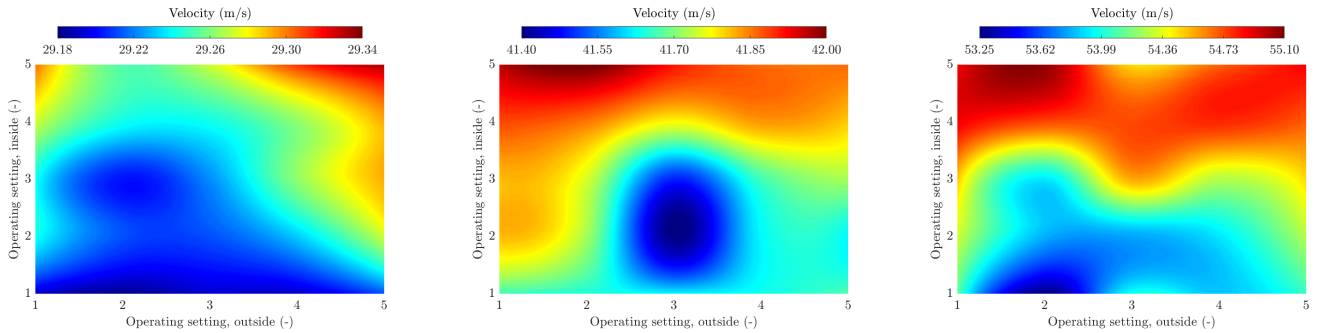
efficients also enhance with increasing outside operating settings. The same response to operating settings for the aerodynamic devices on the opposite side of the vehicle is observed for the outside downforce coefficients, indicating an amplifying aerodynamic interaction between aerodynamic devices on either side of the vehicle occurs.

The distribution of aerodynamic loads, influenced by the operating states of the active aerodynamic devices, induces an aerodynamic roll moment about the vehicle's roll axis. The aerodynamic roll moment coefficients, depicted in Figure 19, therefore provide an indication of the vehicle's AALB capability. In this analysis, positive coefficients refer to an aerodynamic roll moment toward the inside tyres and negative coefficients to an aerodynamic roll moment toward the outside tyres. Hence, a desirable AALB concept in symmetric straight-line conditions would not generate an aerodynamic roll moment at symmetric operating states, whereas inside and outside bias operating states would respectively generate positive and negative aerodynamic roll moments.

The 50L radius corner results show most resemblance to this described straight-line behaviour, where inside and outside bias operating states generally result in positive and negative aerodynamic roll moment coefficients. However, as previously identified, the asymmetric cornering conditions have shown to favour downforce on the inside of the vehicle. Consequently, positive aerodynamic roll moment coefficients are superior, especially in the high operating settings range, as evidenced by the contour line of zero aerodynamic roll. Positive aerodynamic roll moment coefficients become increasingly more dominant with reducing corner radii, corresponding to the high disparity previously seen between the downforce generated on the inside and outside of the vehicle.

The influence of AALB on the maximum cornering velocity of the split rear wing high-performance vehicle concept is presented in Figure 20. Generally, higher cornering velocities are achieved with inside bias compared to outside bias operating states, affirming the respective positive and negative impacts of reducing and amplifying lateral load transfer during cornering. Furthermore, it is noteworthy that prior discussions focused on coefficients of aerodynamic forces and moments to facilitate comparisons between low and high speed cornering conditions. The actual magnitudes of these quantities increase quadratically with the vehicle's velocity. It will therefore become evident in subsequent performance analyses that absolute effects of AALB on the vehicle's cornering performance are larger in high speeds than in low speed corners.

In the 50L radius corner, a peak velocity of 55.09 m/s is achieved at operating state (1.7,5), exceeding the minimum velocity of 53.25 m/s at operating state (2,1) by around 3.5%, and the velocity of 54.87 m/s at the maximum symmetric operating



(a) (b) (c)

Figure 20: Maximum velocity as a function of the operating settings for the inside and outside located active aerodynamic devices of the split rear wing high-performance vehicle concept in the (a) 15L radius corner, (b) 30L radius corner, and (c) 50L radius corner

state (5,5) by about 0.4%. However, the inside bias operating state (1.7,5) achieves the peak velocity by producing approximately 20% less downforce and 16% less drag, reducing the power to overcome aerodynamic drag by about 15% compared to the maximum symmetric operating state.

The peak velocity of 42.01 m/s in the 30L radius corner is reached at operating state (1.8,5), providing an approximate 1.5% improvement over the minimum velocity of 41.40 m/s at operating state (3,2), and 0.4% over the velocity of 41.86 m/s at the maximum symmetric operating state (5,5). Again, the inside bias operating state achieves the peak velocity by generating around 19% less downforce and 16% less drag, using overall about 15% less power to overcome aerodynamic drag.

Performance in the low speed 15L radius corner exhibits the lowest sensitivity to AALB. The cornering velocity seems to primarily benefit from high downforce operating states and relatively independent to inside or outside bias aerodynamic loads. Consequently, a peak velocity of 29.33 m/s is achieved at the maximum symmetric operating state (5,5), increasing the minimum velocity of 29.18 m/s at operating state (2,1) by around 0.5%.

The disparities in performance between the operating states fundamentally originate from the aerodynamic loads generated by the active aerodynamic devices and their subsequent effect on tyre dynamics. This is illustrated in Figure 21, which displays the lateral tyre forces for the maximum symmetric (5,5) and optimal inside bias (1.7,5) operating states in a 50L radius corner.

The core concept behind AALB is to leverage the vertical load sensitivity of the tyres by generating aerodynamic loads that counteract lateral load transfer and prioritise vertical loads on the inside over the outside tyres. This principle is effectively implemented in the inside bias operating state, which decreases lateral load transfer on both axles by approximately 1% compared to the symmetric state, and generates about 1.3 times more downforce on the inside tyres than on the outside tyres, resulting in comparable lateral tyre forces to those of the high downforce symmetric operating state.

The symmetric operating state exhibits understeering limit behaviour, where the front tyres are incapable of producing a larger lateral force if the vehicle's velocity was the increase. Conversely, oversteering limit behaviour is observed for the inside bias operating state, due to the rear tyres' inability to generate a larger lateral force, although the front and rear tyres reach their limit nearly simultaneously.

3.4. Tilted Rear Wing

The downforce and drag coefficients of the tilted rear wing high-performance vehicle concept, presented in Figure 22, mainly increase with higher operating settings for the inside and outside active aerodynamic devices in each cornering condition. The rate at which downforce coefficients increase at low to medium operating settings is highest in the 50L radius corner, whereas the response to high operating settings is most substantial in the 15L radius corner.

The 15L radius corner results also demonstrate noticeable performance fluctuations at high inside and outside bias operating states. These aerodynamic performance variabilities are attributed to the interaction between the tilted rear wing and recirculation wake vortices. These vortex structures have previously been demonstrated to arise in cornering conditions and intensify with reducing corner radii (Rijns et al. (2024b)), thereby only expressing as pronounced performance variations in the 15L radius corner. The interaction seems to be triggered by critical distances between the tilted rear wing and the vehicle body, influenced by the angle of attack and tilt angle settings. The interaction slightly reduces the low-pressure generation underneath the tilted rear wing and increases pressure drag on the vehicle's base, therefore resulting in relatively low downforce with high drag states.

The front axle downforce distribution varies between approximately 50% to 56% throughout the operating states in each cornering condition, thereby remaining within the intended range of the control strategy. Quantitatively, the maximum downforce coefficient in the 15L radius corner is about 4.5% higher than in the 30L and 50L radius corners, while the maximum drag coefficient is less than 1% higher.

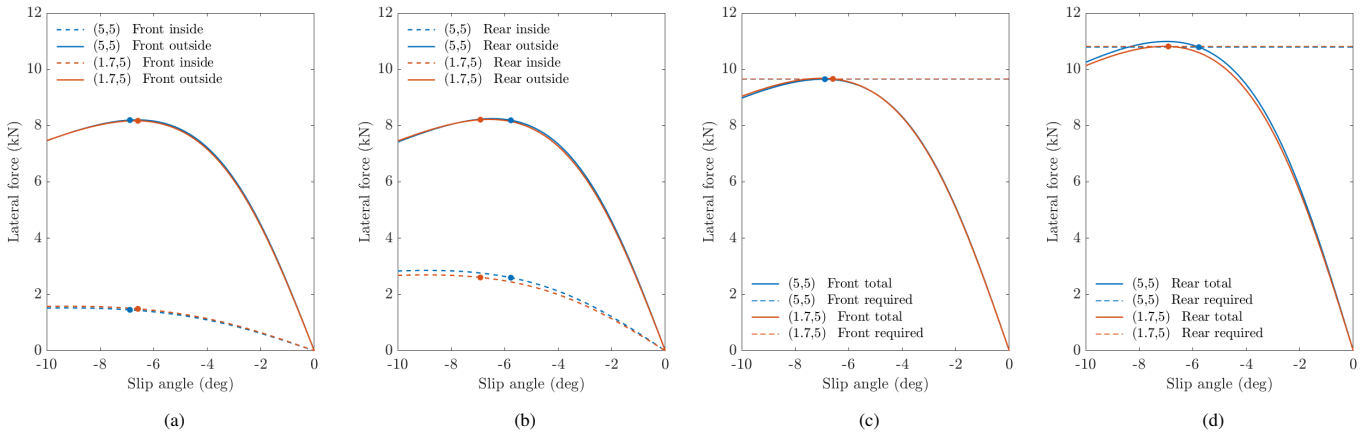
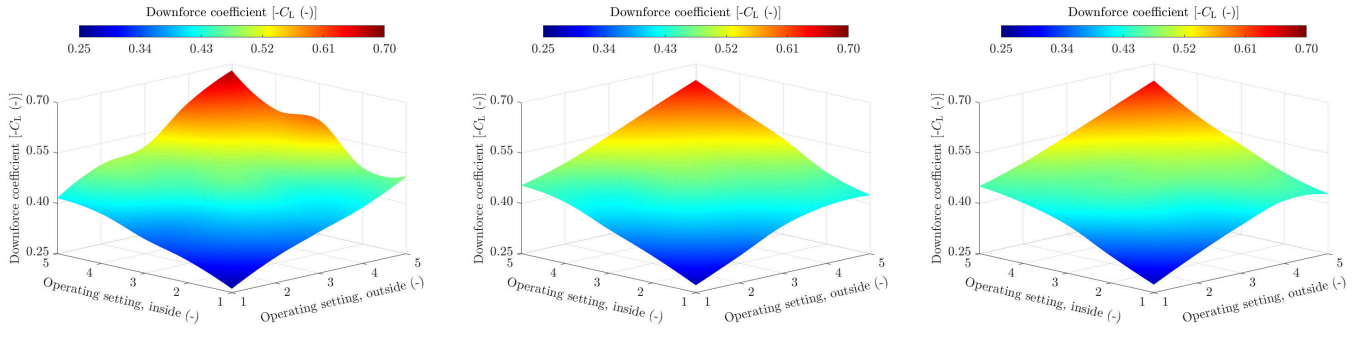
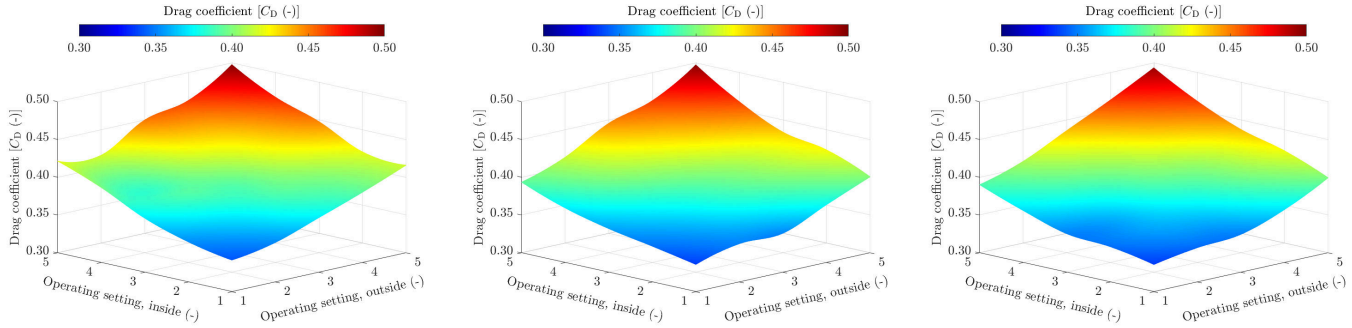


Figure 21: Comparison between the lateral forces produced by the (a) front tyres, (b) rear tyres, (c) front tyres combined, and (d) rear tyres combined of the split rear wing high-performance vehicle concept in its maximum symmetric (5,5) and optimal inside bias (1.7,5) operating states in the 50L radius corner



15L 30L 50L

(a)

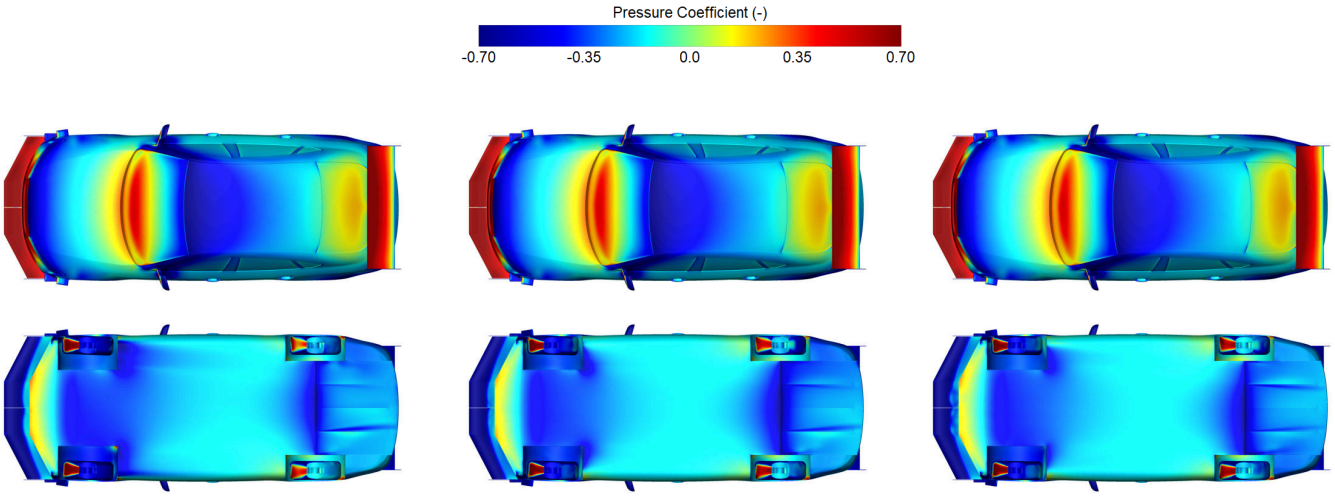


15L 30L 50L

(b)

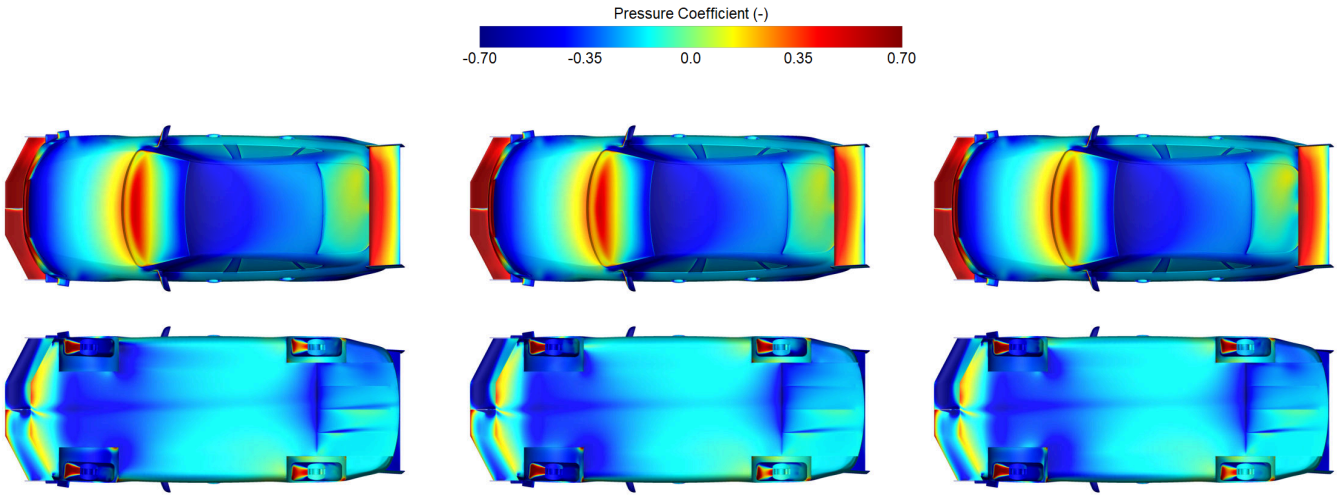
Figure 22: (a) Downforce coefficients and (b) drag coefficients as a function of the operating settings for the inside and outside located active aerodynamic devices of the tilted rear wing high-performance vehicle concept in various cornering conditions

Similarly to the split rear wing concept, pressure coefficient distributions on the maximum symmetric operating state reveal that performance variations across cornering conditions primarily occur on the underbody, as shown in Figure 23. Comparable features like the upstream pressurisation of the rear wing and low-pressure generation on the front wing elements are observable. Furthermore, the downstream development of the low-pressure region near the front axle and the asymmetric pressure distribution in the diffuser again indicate the variation in flow alignment between small and large radius corners.



(a) (b) (c)

Figure 23: Pressure coefficient distribution on the tilted rear wing high-performance vehicle concept in its maximum symmetric operating state (5,5) in the (a) 15L radius corner, (b) 30L radius corner, and (c) 50L radius corner



(a) (b) (c)

Figure 24: Pressure coefficient distribution on the tilted rear wing high-performance vehicle concept in its maximum inside bias operating state (1,5) in the (a) 15L radius corner, (b) 30L radius corner, and (c) 50L radius corner

Pressure coefficient distributions on the maximum inside bias state, presented in Figure 24, depict a relatively symmetric distribution across the tilted rear wing's span, despite its high tilt angle. The upstream pressurisation effect on the other hand is primarily generated by the outside section of the tilted rear wing, which is in closer proximity to the vehicle body, and consequently less considerable than for the maximum symmetric operating state. The increased proximity between the outside section of the tilted rear wing and the vehicle body also induces some local airflow acceleration, slightly promoting flow attachment on the lower surface compared to the wing section which is tilted upwards.

Similar findings to those of the maximum inside bias operating state of the split rear wing concept are observed along the underbody. The low-pressure region on the inside front wing element is more substantial than on the outside element, driving the formation of a vortex which propagates along the floor. Furthermore, front wing operating settings demonstrate to influence downstream flow conditions, where high settings promote the low-pressure generation in the diffuser section on the same side of the vehicle. The low-pressure generation on the inside of the vehicle seems again more evident in smaller corners, likely amplified by previously discussed flow alignment effects.

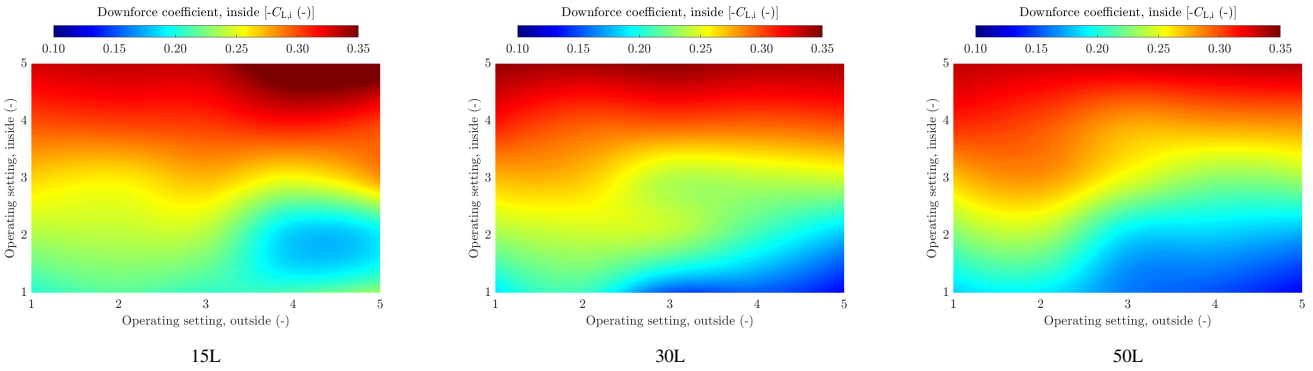
Upon comprehending the operational principles behind the active aerodynamic devices of the tilted rear wing high-performance vehicle concept, Figure 25 shows the impact of the operating states on the downforce exerted on the inside and outside tyres throughout the different cornering conditions. As identified earlier, downforce generation on the inside of the vehicle is somewhat promoted in tight corners, whereas more symmetrically distributed aerodynamic loads are generated in large radius corner which approximate symmetric straight-line conditions. Consequently, an increasing variability in the magnitudes of inside and outside downforce coefficients is observed with reducing corner radii.

Throughout the cornering conditions, inside and outside downforce coefficients increase with higher operating settings for the active aerodynamic devices on the respective sides of the vehicle. However, the inside downforce coefficients demonstrate to reduce with higher outside operating settings for a constant inside operating setting and vice versa. This response is to be expected since the aerodynamic load bias to a single side of the vehicle reduces when the opposite operating setting is increased, generating more laterally balanced aerodynamic loads.

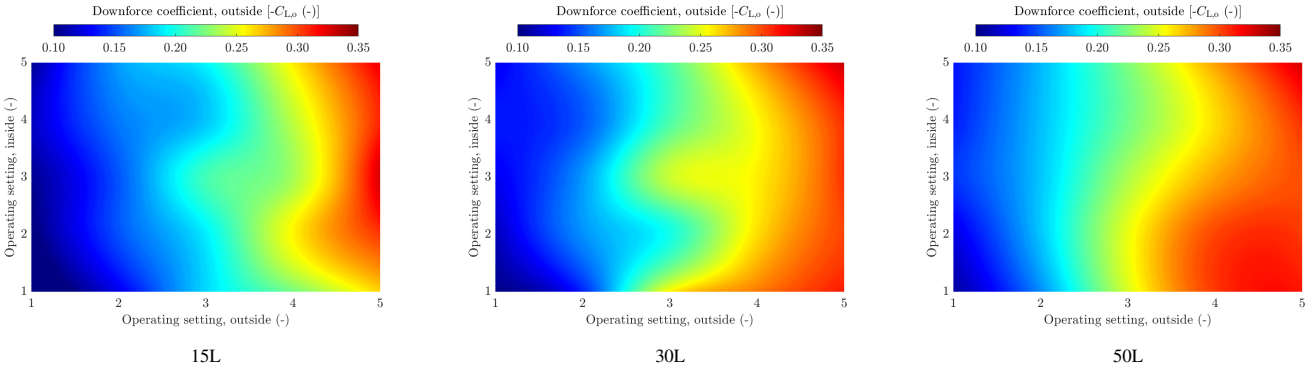
The aerodynamic load distribution induces an aerodynamic roll moment about the vehicle roll axis, as presented in Figure 26, which provides insights into the vehicle's AALB capability. As mentioned before, positive coefficients refer to an aerodynamic roll moment toward the inside tyres and negative coefficients to an aerodynamic roll moment toward the outside tyres in this analysis. In straight-line conditions, a desired AALB concept with symmetric settings would not generate an aerodynamic roll moments, whereas inside and outside bias operating states would generate positive and negative aerodynamic roll moments.

Aerodynamic roll moment coefficients in the 50L radius corner are nearly identical to the desired response in straight-line conditions described above. The contour line of zero aerodynamic roll is however marginally below the diagonal with symmetric operating states, since the slight asymmetric conditions in this large corner radius still favour an inside bias aerodynamic load distribution. As previously identified, the bias toward inside downforce generation increases with reducing corner radii, also evidenced from the increasing positive aerodynamic roll moment coefficients across the operating states in tighter corners.

The impact of AALB on the maximum cornering velocity of the tilted rear wing high-performance vehicle concept is provided in Figure 27. Evidently, higher cornering velocities are



(a)

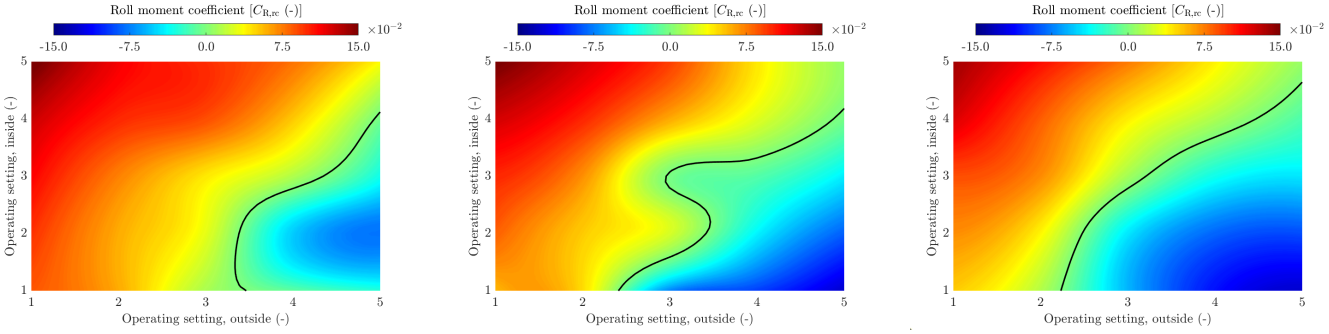


(b)

Figure 25: Downforce coefficients on the (a) inside tyres and (b) outside tyres as a function of the operating settings for the inside and outside located active aerodynamic devices of the tilted rear wing high-performance vehicle concept in various cornering conditions

generally observed for inside bias compared to outside bias operating states for each cornering condition. This emphasises the respective performance enhancing and deteriorating effects of counteracting or reinforcing lateral load transfer during cornering. As previously noted, the actual magnitudes of aerodynamic forces and moments increase quadratically with the vehicle's velocity as opposed to their respective coefficients discussed above. Hence, subsequent performance analyses will demonstrate larger absolute effects of AALB on cornering performance in high speed corners compared to low speed corners.

In the 50L radius corner, the maximum inside bias operating state (1,5) provides a peak velocity of 55.73 m/s, which is approximately 6.4% higher than the minimum velocity of 52.38 m/s at operating state (5,1), and 1.7% higher than the velocity of 54.79 m/s at the maximum symmetric operating state (5,5). The maximum inside bias operating state generates about 28% less downforce and 18% less drag, thereby achieving the peak cornering velocity using around 18% less power to overcome aerodynamic drag compared to the maximum symmetric operating state.



(a) (b) (c)

Figure 26: Aerodynamic roll moment coefficients about the vehicle's roll axis as a function of the operating settings for the inside and outside located active aerodynamic devices of the tilted rear wing high-performance vehicle concept in the (a) 15L radius corner, (b) 30L radius corner, and (c) 50L radius corner. The black contour lines mark an aerodynamic roll moment coefficient of zero.

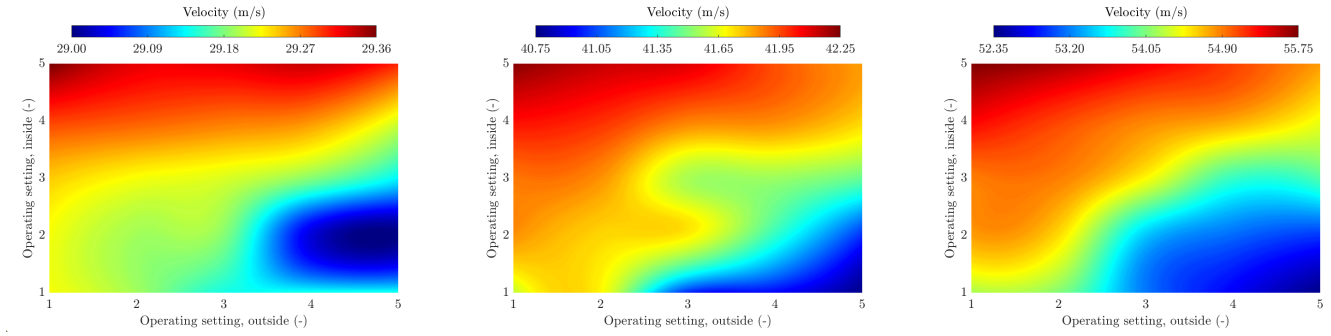


Figure 27: Maximum velocity as a function of the operating settings for the inside and outside located active aerodynamic devices of the tilted rear wing high-performance vehicle concept in the (a) 15L radius corner, (b) 30L radius corner, and (c) 50L radius corner

The maximum inside bias operating state (1,5) produces a peak velocity of 42.23 m/s in the 30L radius corner, exceeding the minimum velocity of 40.76 m/s at operating state (5,1) by about 3.6%, and the velocity of 41.82 m/s at the maximum symmetric operating state (5,5) by 1%. Hence, peak velocity at the maximum inside bias operating state is achieved using approximately 29% less downforce and 19% less drag, reducing the power to overcome aerodynamic drag by around 18% compared to the maximum symmetric operating state.

The peak velocity of 29.36 m/s in the 15L radius corner is again achieved at the maximum inside bias operating state (1,5), providing an approximate 1.3% improvement over the minimum velocity of 29.00 m/s at operating state (4.8,2), and 0.2% over the velocity of 29.30 m/s at the maximum symmetric operating state (5,5). The maximum inside bias operating state produces around 38% less downforce and 15% less drag, thereby delivering the peak cornering velocity using about 15% less power to overcome aerodynamic drag compared to the maximum symmetric operating state.

As previously discussed, variations in cornering performance are primarily attributed to the aerodynamic loads generated by active aerodynamic devices and their subsequent influence on tyre behaviour. To provide a more detailed analysis of tyre dynamics, the lateral tyre forces for both the maximum symmetric (5,5) and optimal inside bias (1,5) operating states in a 50L radius corner are depicted in Figure 28. Through the application of AALB, the inside bias operating state effectively reduces the lateral load transfer across both axles by approximately 3% compared to the symmetric state, and generates about 2.5 times more downforce on the inside than on the outside tyres.

It is important to highlight that a high tilt angle of the rear wing not only generates a vertical force but also a horizontal force component, which primarily contributes to the lateral force exerted at the rear axle. As a result, even though the inside bias operating state necessitates the generation of a larger total lateral force to maintain its cornering trajectory due to its increased velocity, it is evident that the required force at the rear wheels is diminished in comparison to the symmetric operating state, owing to the substantial aerodynamic side force generated by the tilted rear wing.

For both the inside bias and symmetric operating state, the front tyres would be unable to generate a larger lateral force if the vehicle's velocity was to increase, leading to understeering limit behaviour.

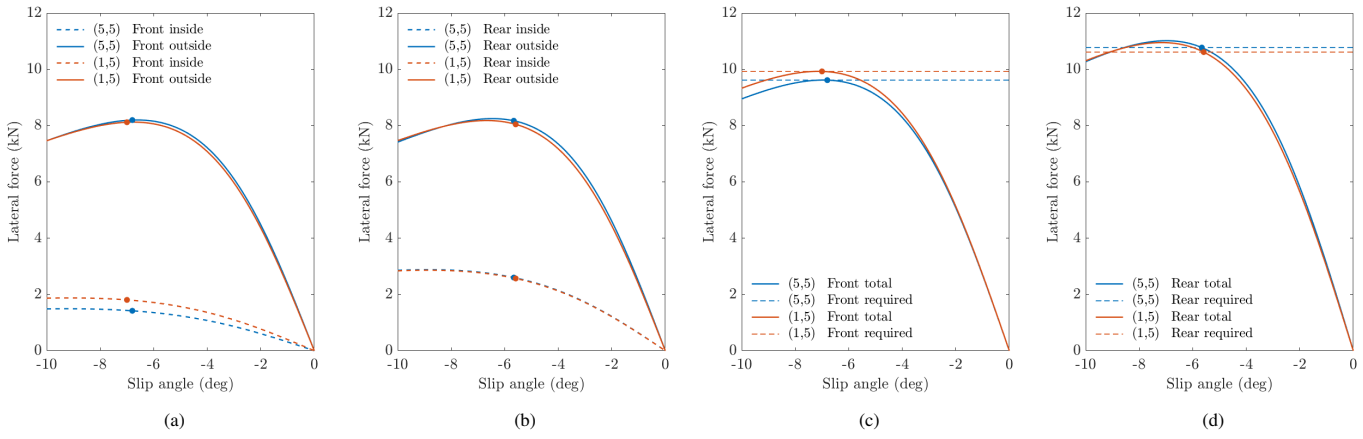


Figure 28: Comparison between the lateral forces produced by the (a) front tyres, (b) rear tyres, (c) front tyres combined, and (d) rear tyres combined of the tilted rear wing high-performance vehicle concept in its maximum symmetric (5,5) and optimal inside bias (1,5) operating states in the 50L radius corner

3.5. Split Rear Wing vs Tilted Rear Wing

The split rear wing and tilted rear wing high-performance vehicle concepts both aim to enhance cornering performance by controlling vertical tyre forces through AALB. However, the underlying mechanisms to achieve AALB and the subsequent efficacy in improving cornering performance differ between these concepts.

The split rear wing concept primarily influences the aerodynamic load distribution by the amount of aerodynamic force generated vertically on either side of the vehicle. In contrast, the tilted rear wing concept is able to generate substantial aerodynamic forces in both vertical and horizontal directions, resulting in a range of aerodynamic roll moment coefficients that is double that of the split rear wing concept.

Both concepts generate favourable downforce on the vehicle's inside due to asymmetric flow conditions during cornering, resulting in a positive aerodynamic roll moment. However, the tilted rear wing concept provides a more desirable response to the control strategy than the split rear wing concept. It demonstrates a more consistent transition of positive to negative aerodynamic roll moment coefficients at respective inside bias and outside bias operating states across the cornering conditions. This consistency is less evident in the split rear wing concept, due to increased flow interactions between the split elements.

In terms of performance, the tilted rear wing concept outperforms the split rear wing concept by achieving higher cornering velocities through its superior AALB capability. Specifically, it attains an approximate 1.2% higher maximum velocity in the 50L radius corner, while using nearly 10% less downforce and 2% less drag. In the 30L radius corner, the tilted rear wing's maximum velocity is around 0.5% higher, achieved with approximately 12% less downforce and 2% less drag.

In the 15L radius corner, both concepts reach similar maximum velocities. However, the split rear wing needs to operate at the maximum downforce state to reach its peak velocity in such low speed corners due to its limited AALB capability. In contrast, the tilted rear wing, with its enhanced AALB capability, reaches its peak velocity at the maximum inside bias operating state. This results in a comparable cornering velocity, but with approximately 39% less downforce and 14% less drag.

4. Conclusion

This study investigated the potential of active aerodynamic load balancing (AALB) on improving the cornering performance of high-performance vehicles. The AALB capabilities of two high-performance vehicle concepts, equipped with an active split front wing and either a split rear wing or tilted rear wing, were analysed and compared to provide insights into the efficacy of these active aerodynamic devices.

The cornering performance was evaluated through a quasi-steady static coupling of the vehicle's aerodynamics and dynamics. This methodology considered aerodynamic loads, lateral load transfer, and non-linear tyre characteristics to determine the maximum cornering velocity. The aerodynamic data for the active high-performance vehicle concepts were obtained under representative operating conditions, ensured by an initial performance assessment of a baseline high-performance vehicle based on wind tunnel measurements.

Sufficient levels of AALB were achieved by both the split rear wing and tilted rear wing concepts to noticeably influence cornering performance. The findings supported the initial hypothesis of this research, demonstrating that inside bias operating states, intended to promote downforce on the inside tyres and counteract effects of lateral load transfer, improve cornering performance. In contrast, outside bias operating states, which favour downforce on the outside tyres and reinforce effects of lateral load transfer, were shown to deteriorate cornering performance.

The performance improvements were found to become more substantial in high speed corners, due to the quadratic increase of aerodynamic forces with the vehicle's velocity. Optimal inside bias operating states of the split rear wing and tilted rear wing concepts were able to reach approximately 0.5% and 2% higher velocities in the highest-speed corner than the maximum symmetric operating states, respectively. Notably, through effectively distributing the aerodynamic loads, the optimal inside bias operating states achieved peak velocities using less downforce and drag compared to the maximum symmetric operating states. Consequently, the propulsion power to overcome drag was also reduced in each cornering condition by about 15%-20%.

Comparing both high-performance vehicle concepts, the titled rear wing outperformed the split rear wing in terms of its ability to influence the aerodynamic load distribution and achieving peak cornering performance. It was able to generate two times larger aerodynamic roll moments, and exhibited a more consistent response to the control strategy with a more direct relation between the bias of an operating state and the aerodynamic roll moment magnitude.

The superior AALB capability was attributed to the tilted rear wing's ability to generate both vertical and horizontal aerodynamic force components to influence the aerodynamic distribution. Conversely, the split rear wing concept was only able influence the aerodynamic load distribution by varying the magnitude of aerodynamic forces in the vertical direction on either side of the vehicle. As a result, the tilted rear wing concept achieved the highest maximum cornering velocities, while using less propulsion power to overcome drag in each of the considered cornering conditions.

Overall, this research demonstrated the significant potential of utilising AALB through active asymmetric aerodynamic devices for enhancing cornering performance. The findings offered crucial insights into the underlying principles of AALB and the fundamental design mechanisms beneficiary for effective control over aerodynamic loads. These results establish the foundation for future work on advanced active aerodynamic solutions for enhancing the performance and efficiency of next-generation high-performance and automotive vehicles. Explorations considering other dynamic conditions or alternative control strategies could lead to new insights and potentially even greater performance gains, guiding the development of ad-

vanced and efficient vehicles.

Acknowledgements

The authors would like to thank the technicians from the 8x6 Wind Tunnel at Cranfield University for their valuable support during the wind tunnel experiments.

Conflict of Interest Statement

The authors have no conflicts to disclose.

Data Availability Statement

The experimental data that support the findings of this study are openly available in Cranfield Online Research Data at https://doi.org/10.17862/cranfield.rd.25721697 (Rijns et al. (2024c)).

References

B. J. Adam Brandt and S. Sebben. High speed driving stability of road vehicles under crosswinds: an aerodynamic and vehicle dynamic parametric sensitivity analysis. *Vehicle System Dynamics*, 60(7):2334–2357, 2022. doi: 10.1080/00423114.2021.1903516.

A. H. Ahangarnejad and S. Melzi. Numerical analysis of the influence of an actively controlled spoiler on the handling of a sports car. *Journal of Vibration and Control*, 24(22):5437–5448, 2018. doi: 10.1177/1077546318754683.

C. Albukrek, P. Doddegowda, A. Ivaldi, J. Amodeo, and E. Bardoscia. Unsteady flow analysis of a formula type open wheel race car in cornering. In *Motorsports Engineering Conference Exposition*. SAE International, dec 2006. doi: https://doi.org/10.4271/2006-01-3661.

Avon Tyres. Technical data resources, 2024. URL `https://www.avontyres.com/en-gb/tyre-care/motorsport-technical-data/technical-data-resources/`. Accessed: 2024-04-12.

D. T. Ayyagari and Y. He. Aerodynamic analysis of an active rear split spoiler for improving lateral stability of high-speed vehicles. *International Journal of Vehicle Systems Modelling and Testing*, 12(3-4):217–239, 2017. doi: 10.1504/IJVSMT.2017.089978.

J. Broniszewski and J. Piechna. A fully coupled analysis of unsteady aerodynamics impact on vehicle dynamics during braking. *Engineering Applications of Computational Fluid Mechanics*, 13(1):623–641, 2019. doi: 10.1080/19942060.2019.1616326.

J. Broniszewski and J. Piechna. Fluid-structure interaction analysis of a competitive car during brake-in-turn manoeuvre. *Energies*, 15(8):2917, 2022. doi: https://doi.org/10.3390/en15082917.

J. Cai, S. Kapoor, T. Sikder, and Y. He. Effects of active aerodynamic wings on handling performance of high-speed vehicles. In *WCX 17: SAE World Congress Experience*. SAE International, mar 2017. doi: https://doi.org/10.4271/2017-01-1592.

L. Carbonne, N. Winkler, and G. Efraimsson. Use of full coupling of aerodynamics and vehicle dynamics for numerical simulation of the crosswind stability of ground vehicles. sep 2016. ISSN 1946-391X. doi: https://doi.org/10.4271/2016-01-8148.

F. Diba, A. Barari, and E. Esmailzadeh. Handling and safety enhancement of race cars using active aerodynamic systems. *Vehicle System Dynamics*, 52 (9):1171–1190, 2014. doi: 10.1080/00423114.2014.930158.

J. C. Dixon. *Tires, Suspension and Handling, Second Edition*. SAE International, sep 1996.

D. C. Forbes. Coupling road vehicle aerodynamics and dynamics in simulation. 2017. URL `https://repository.lboro.ac.uk/articles/thesis/Coupling_road_vehicle_aerodynamics_and_dynamics_in_simulation/9214619`.

D. C. Forbes, G. J. Page, M. A. Passmore, and A. P. Gaylard. A fully coupled, 6 degree-of-freedom, aerodynamic and vehicle handling crosswind simulation using the drivaer model. *SAE International Journal of Passenger Cars - Mechanical Systems*, 9(2):710–722, apr 2016. ISSN 1946-3995. doi: https://doi.org/10.4271/2016-01-1601.

M. Hammad, K. Qureshi, and Y. He. Safety and lateral dynamics improvement of a race car using active rear wing control. In *WCX SAE World Congress Experience*. SAE International, apr 2019. doi: https://doi.org/10.4271/2019-01-0643.

A. Heft, T. Indinger, and N. Adams. Introduction of a new realistic generic car model for aerodynamic investigations. *SAE Technical Paper 2012-01-0168*, 04 2012. doi: https://doi.org/10.4271/2012-01-0168.

E. Josefsson, R. Hagvall, M. Urquhart, and S. Sebben. Numerical analysis of aerodynamic impact on passenger vehicles during cornering. In *CO2 Reduction for Transportation Systems Conference*. SAE International, may 2018. doi: https://doi.org/10.4271/2018-37-0014.

J. Keogh. *The Aerodynamic Effects of the Cornering Flow Conditions*. PhD thesis, School of Mechanical and Manufacturing Engineering, University of New South Wales, 2016.

J. Keogh, T. Barber, S. Diasinos, and G. Doig. The aerodynamic effects on a cornering ahmed body. *Journal of Wind Engineering and Industrial Aerodynamics*, 154:34–46, 2016. ISSN 0167-6105. doi: https://doi.org/10.1016/j.jweia.2016.04.002.

R. Kono, T. Nakashima, M. Tsubokura, Y. Okada, and T. Nouzawa. Aerodynamics simulation of a sedan-type road vehicle in cornering motion with roll angle. In *34th AIAA Applied Aerodynamics Conference*. American Institute of Aeronautics and Astronautics, 2016. doi: https://doi.org/10.2514/6.2016-3726.

K. Kurec, M. Remer, J. Broniszewski, P. Bibik, S. Tudruj, and J. Piechna. Advanced modeling and simulation of vehicle active aerodynamic safety. *Journal of Advanced Transportation*, 2019(Article ID 7308590), 2019a. doi: https://doi.org/10.1155/2019/7308590.

K. Kurec, M. Remer, T. Mayer, S. Tudruj, and J. Piechna. Flow control for a car-mounted rear wing. *International Journal of Mechanical Sciences*, 152: 384–399, 2019b. ISSN 0020-7403. doi: https://doi.org/10.1016/j.ijmecsci.2018.12.034.

M. Lanfrit. Best practice guidelines for handling automotive external aerodynamics with fluent. 2005. Fluent Deutschland GmbH.

M. T. Lin and P. Papadopoulos. Race car aerodynamics simulation and transmitted tire reaction forces. *International Journal of Automotive Engineering*, 13(4):169–176, 2022. doi: 10.20485/jsaeijae.13.4_169.

N. J. Mckay and A. Gopalarathnam. The effects of wing aerodynamics on race vehicle performance. In *Motorsports Engineering Conference Exhibition*. SAE International, dec 2002. doi: https://doi.org/10.4271/2002-01-3294.

F. R. Menter. Two-equation eddy-viscosity turbulence models for engineering applications. *AIAA Journal*, 32(8):1598–1605, 1994. doi: https://doi.org/10.2514/3.12149.

T. Nakashima, M. Tsubokura, S. Matsuda, and Y. Doi. *Coupled Analysis of Unsteady Aerodynamics and 6DoF Motion of a Heavy Duty Truck in Strong Wind Gusts*. 2011. doi: 10.2514/6.2011-3672.

T. Nakashima, M. Tsubokura, M. Vázquez, H. Owen, and Y. Doi. Coupled analysis of unsteady aerodynamics and vehicle motion of a road vehicle in windy conditions. *Computers Fluids*, 80:1–9, 2013. ISSN 0045-7930. doi: https://doi.org/10.1016/j.compfluid.2012.09.028. URL `https://www.sciencedirect.com/science/article/pii/S0045793012004094`. Selected contributions of the 23rd International Conference on Parallel Fluid Dynamics ParCFD2011.

T. Nakashima, M. Tsubokura, Y. Okada, T. Nouzawa, R. Kono, and Y. Doi. Aerodynamic characteristics of a road vehicle in steady-state cornering. In *Proceedings of the ASME/JSME/KSME 2015 Joint Fluids Engineering Conference. Volume 1A: Symposia, Part 2*. The American Society of Mechanical Engineers, 2015. doi: https://doi.org/10.1115/AJKFluids2015-17553.

T. Nakashima, H. Mutsuda, T. Kanehira, and M. Tsubokura. Fluid-dynamic force measurement of ahmed model in steady-state cornering. *Energies*, 13 (24), 2020. ISSN 1996-1073. doi: 10.3390/en13246592.

K. Nara, M. Tsubokura, and J. Ikeda. *A Numerical Analysis of Unsteady Aerodynamics of Formula Car During Dynamic Cornering Motion*. 2014. doi: https://doi.org/10.2514/6.2014-3138.

H. B. Pacejka. *Tire and Vehicle Dynamics*. Butterworth-Heinemann, Oxford, third edition edition, 2012. ISBN 978-0-08-097016-5. doi: https://doi.org/10.1016/B978-0-08-097016-5.00001-2.

J. R. Piechna, K. Kurec, J. Broniszewski, M. Remer, A. Piechna, K. Kamieniecki, and P. Bibik. Influence of the car movable aerodynamic elements on fast road car cornering. *Energies*, 15(3), 2022. ISSN 1996-1073.

S. Rijns, T.-R. Teschner, K. Blackburn, and J. Brighton. Aerodynamic analysis of the ride height dependency of a high-performance vehicle equipped with a multichannel diffuser in ground effect. *SAE Technical Paper 2023-01-5064*, sep 2023. ISSN 0148-7191. doi: https://doi.org/10.4271/2023-01-5064.

S. Rijns, T.-R. Teschner, K. Blackburn, and J. Brighton. Integrated numerical and experimental workflow for high-performance vehicle aerodynamics. *SAE Technical Paper 2024-01-5016*, 2024a. ISSN 0148-7191. doi: https://doi.org/10.4271/2024-01-5016.

S. Rijns, T.-R. Teschner, K. Blackburn, and J. Brighton. Effects of cornering conditions on the aerodynamic characteristics of a high-performance vehicle and its rear wing. *Physics of Fluids*, 36(4):045119, 04 2024b. ISSN 1070-6631. doi: 10.1063/5.0204204.

S. Rijns, T.-R. Teschner, K. Blackburn, and J. Brighton. Dataset drivaer hp-f: Force measurements at various rear wing angles of attack. 2024c. doi: 10.17862/cranfield.rd.25721697. URL `https://cord.cranfield.ac.uk/articles/dataset/Dataset_DrivAer_hp-F_Force_Measurements_at_Various_Rear_Wing_Angles_of_Attack/25721697`.

S. Rijns, T.-R. Teschner, K. Blackburn, A. R. Proenca, and J. Brighton. Experimental and numerical investigation of the aerodynamic characteristics of high-performance vehicle configurations under yaw conditions. *Physics of Fluids*, 36(4):045112, 04 2024d. ISSN 1070-6631. doi: 10.1063/5.0196979.

J. W. Saunders and R. B. Mansour. On-road and wind tunnel turbulence and its measurement using a four-hole dynamic probe ahead of several cars. In *SAE 2000 World Congress*. SAE International, 2000. doi: https://doi.org/10.4271/2000-01-0350.

D. Seward. *Race car design*. PALGRAVE, 2014. ISBN 978-1-137-03014-6.

T. Sikder, S. Kapoor, and Y. He. Optimizing Dynamic Performance of High-Speed Road Vehicles Using Aerodynamic Aids. volume Volume 7: Fluids Engineering of *ASME International Mechanical Engineering Congress and Exposition*, page V007T09A060, 11 2016. doi: 10.1115/IMECE2016-65414.

R. F. Soares, A. Knowles, S. G. Olives, K. Garry, and J. C. Holt. On the aerodynamics of an enclosed-wheel racing car: An assessment and proposal of add-on devices for a fourth, high-performance configuration of the drivaer model. *SAE Technical Paper 2018-01-0725*, April 2018. doi: https://doi.org/10.4271/2018-01-0725.

M. Szudarek and J. Piechna. Cfd analysis of the influence of the front wing setup on a time attack sports car's aerodynamics. *Energies*, 14(23), 2021. ISSN 1996-1073. doi: https://doi.org/10.3390/en14237907.

T. Tunay. Two-way coupled aerodynamics and vehicle dynamics simulations of a heavy ground vehicle subjected to crosswind of various frequencies. *Proceedings of the Institution of Mechanical Engineers, Part D: Journal of Automobile Engineering*, 237(6):1406–1422, 2023. doi: 10.1177/09544070221088070.

T. Tunay, E. Firat, and B. Sahin. Experimental investigation of the flow around a simplified ground vehicle under effects of the steady crosswind. *International Journal of Heat and Fluid Flow*, 71:137–152, 2018. ISSN 0142-727X. doi: https://doi.org/10.1016/j.ijheatfluidflow.2018.03.020.

E. Velenis, E. Frazzoli, and P. Tsiotras. Steady-state cornering equilibria and stabilisation for a vehicle during extreme operating conditions. *International Journal of Vehicle Autonomous Systems*, 8:217–241, 2010.

N. Winkler, L. Drugge, A. S. Trigell, and G. Efraimsson. Coupling aerodynamics to vehicle dynamics in transient crosswinds including a driver model. *Computers Fluids*, 138:26–34, 2016. ISSN 0045-7930. doi: https://doi.org/10.1016/j.compfluid.2016.08.006. URL `https://www.sciencedirect.com/science/article/pii/S004579301630250X`.

D. Zavala, W. Vicente, R. Esquivel, and M. Salinas-Vazquez. Numerical simulation of the effect of a centripetal wing spoiler on the flow aerodynamics of a sports car. *SAE Technical Paper 2023-01-5032*, 2023. ISSN 0148-7191. doi: https://doi.org/10.4271/2023-01-5032.



https://dspace.org/

Performance analyses of active aerodynamic load balancing designs on high-performance vehicles in cornering conditions

Rijns, Steven; Teschner, Tom-Robin; Blackburn, Kim; Brighton, James

2024-08-29
American Institute of Physics (AIP)
https://doi.org/10.1063/5.0222780
Rijns S, Teschner T-R, Blackburn K, Brighton J. (2024) Performance analyses of active aerodynamic load balancing designs on high-performance vehicles in cornering conditions. Physics of Fluids, Volume 36, Issue 8, August 2024, Article number 085199

Downloaded from a DSpace repository. https://dspace.org/